ARTICLES
https://doi.org/10.1038/s41477-021-00931-z

nature plants

Real-time conversion of tissue-scale mechanical forces into an interdigitated growth pattern

Samuel A. Belteton[1], Wenlong Li[2], Makoto Yanagisawa[3], Faezeh A. Hatam[2], Madeline I. Quinn[1], Margaret K. Szymanski[4], Matthew W. Marley[1], Joseph A. Turner[2] and Daniel B. Szymanski[1,5]✉

The leaf epidermis is a dynamic biomechanical shell that integrates growth across spatial scales to influence organ morphology. Pavement cells, the fundamental unit of this tissue, morph irreversibly into highly lobed cells that drive planar leaf expansion. Here, we define how tissue-scale cell wall tensile forces and the microtubule–cellulose synthase systems dictate the patterns of interdigitated growth in real time. A morphologically potent subset of cortical microtubules span the periclinal and anticlinal cell faces to pattern cellulose fibres that generate a patch of anisotropic wall. The subsequent local polarized growth is mechanically coupled to the adjacent cell via a pectin-rich middle lamella, and this drives lobe formation. Finite element pavement cell models revealed cell wall tensile stress as an upstream patterning element that links cell- and tissue-scale biomechanical parameters to interdigitated growth. Cell lobing in leaves is evolutionarily conserved, occurs in multiple cell types and is associated with important agronomic traits. Our general mechanistic models of lobe formation provide a foundation to analyse the cellular basis of leaf morphology and function.

Leaves are specialized planar organs optimized for photosynthesis and gas exchange. Their anatomy varies wildly and reflects complex interactions between the environment and the life cycle[1]. The epidermis functions as a biomechanical shell that controls the growth properties at organ scales[2–4], and the size and shape of leaves are ultimately determined by the slow, irreversible expansion of pavement cells[5,6]. A lobed pavement cell morphology is an evolutionarily conserved feature[7], and interdigitated growth drives organ expansion and probably increases the mechanical toughness of large, thin leaves. Despite the widespread occurrence and broad importance of lobed morphogenesis, how this polarized growth process occurs is a long-standing and controversial research question[8–13].

Numerous and varied explanations for the mechanism of lobe formation have been proposed[9,11,14–18]. The extreme heterogeneity in pavement cell development is one contributing factor. Cells with only subtle undulations and those with a highly convoluted shape coexist in the same leaf sectors for the lifespan of the organ. Historically, cell behaviours were surmised on the basis of static images from populations of cells[9]. However, the growth trajectories of pavement cells cannot be predicted from static images[13,19], making it impossible to attribute a given pattern of protein localization[10] or cell wall tensile force[16,20] to shape change. More recent analyses used time-lapse measurements to analyse pavement cell growth[15,17,19,21,22]. However, lobes originate as local ~300 nm deflections in the anticlinal wall and appear in the timescale of tens of minutes[13], and no parameter or protein has been proven to control lobe formation. Lobed cells, like others that employ a polarized diffuse growth mechanism, use microtubule-dependent templating of cellulose fibres in the cell wall[23] to pattern anisotropic expansion[9,11,24]. However, in general, there is a lack of clarity about which subsets of microtubules are morphologically potent. Furthermore, a common assumption is that diffuse growth in plant cells is uniform across the entire cell surface area[25]. However, subcellular growth pattern analyses in several cell types[19,26] suggest that this might be the exception rather than the rule.

In pavement cells, long-standing models propose that stable microtubules synthesize cellulose arrays or cell wall thickenings that locally restrict growth and cause lobe outgrowths to appear at adjacent subdomains of the cell[9,16]. In *Arabidopsis*, the microtubule system is unstable, and anticlinal microtubule bundling is not associated with local cell wall thickening[13,27]. An alternative growth-promotion model proposes that localized microtubule arrays pattern cellulose microfibrils to generate a patch of local anisotropic expansion that drives symmetry breaking[11]. Even in pavement cells with existing lobes, the mechanism by which microtubules promote lobe outgrowth is also unclear. The qualitative enrichment of splayed cortical microtubules at convex cell surfaces has been highlighted in different types of growth-restriction models[9,15,16,20]. However, microtubules are only sporadically enriched along subsets of seemingly equivalent convex cell surfaces, and the role of microtubules in lobe outgrowth is unclear[27].

Additional distinct explanations of interdigitated growth have recently emerged based primarily on the outputs of biomechanical simulations of pavement cells or cell wall components[17,18,28,29]. The finite element (FE) modelling approach is well suited to analysing plant cell morphogenesis because it simulates stress–strain relationships of thin-walled pressurized shells and can be adapted to any cell geometry[26,30]. Because the material properties and rheology of the cell wall are unknown in most cell types, this approach can make useful predictions. However, the primary liability is that the FE model outputs are highly sensitive to geometry and user-defined variables related to unknown cell wall material properties[17,28,29]. Another pectin-centric model, based on vertical bands of pectin in the anticlinal wall[18], predicts that the hydration forces of pectic nanofibres cause local cell protrusion. The simulation studies above generated divergent solutions in part because key parameters varied greatly from one model to the next and model predictions were not adequately validated with experimental data.

[1]Department of Botany and Plant Pathology, Purdue University, West Lafayette, IN, USA. [2]Mechanical and Materials Engineering, University of Nebraska–Lincoln, Lincoln, NE, USA. [3]Department of Botany, University of Wisconsin, Madison, WI, USA. [4]Department of Biochemistry, Indiana University Bloomington, Bloomington, IN, USA. [5]Biological Sciences, Purdue University, West Lafayette, IN, USA. ✉e-mail: szymandb@purdue.edu

Here we developed new live-cell imaging and cross-correlation approaches to discover the mechanisms of lobe formation and outgrowth. The multichannel imaging pipeline was used to accurately graph cell shape and microtubule behaviours at ten-minute intervals for hours, revealing potent transfacial microtubules that accurately predict lobe initiation sites. Combinations of mutants, inhibitors and FE modelling were used to show that the microtubule–cellulose systems in an 'initiating' cell drive symmetry breaking. Pectin-based adhesion at the cell–cell interface locally couples polarized growth to the adjacent 'following' cell to enable interdigitated growth. An FE model based on cell wall properties validated with nanoindentation experiments was used to show that tensile forces in the cell wall provide multiscale patterning information to localize morphologically powerful microtubules. These results explain how mechanical forces, cytoskeletal systems and cell wall systems pattern tissue morphogenesis and provide a general explanation for lobe formation in plant cells with a cellulose-rich cell wall.

Results

Heterogeneous growth and wall tensile force patterns of developing pavement cells. The initial growth analyses focused on the behaviours and properties of the anticlinal wall since it directly reflects shape change, and because growth-restriction models predict that the apical regions of lobes are slow growing[9,15,16,20]. To directly test for subcellular strain gradients in the anticlinal wall, we developed a two-channel, three-dimensional (3D) long-term time-lapse imaging pipeline. Cell shape at the anticlinal–periclinal wall interface was accurately quantified with the plasma membrane marker PIP2–mCherry, and local strain gradients were measured using the plasmodesmata-localized protein PDLP3–GFP a fiducial mark (Fig. 1a–c and Supplementary Video 1). Tracking the plasma membrane coordinates between two three-way cell wall junctions made it apparent that lobe height and width and the length of the adjacent anticlinal wall all increased over time (Fig. 1d), a shape change pattern that is consistent with broadly distributed and coordinated cell growth along the lobed cell–cell interface. Segment growth was anisotropic because the boundary changed in shape over the time course (Fig. 1e).

We used PDLP3-marked plasmodesmata as fiducial marks to test for growth rate gradients and correlations with cell shape. Externally applied beads can be used to mark exposed outer periclinal cell surfaces[19], but it is not possible to get the uniform, high-density labelling needed for statistical analyses. The displacement of paired trackable particles, including the three-way junctions, were measured at 15 or 30 min intervals for 4.5 to 6 h (Extended Data Fig. 1a–f), and the PDLP3 displacements depended on tissue growth (Extended Data Fig. 1g–l). Subsegment growth rates were reliable because in all validated cases, the sum of subsegment strains was within 3% of the growth rate that was measured independently using the terminal three-way junctions. There was a high degree of heterogeneity within individual segments (Fig. 1f and Extended Data Fig. 2j). These results conflict with a previous growth-restriction model that assumed anticlinal wall growth rates were uniform along the cell perimeter[15]. To determine whether there were differences in the growth rates of lobe apex or flanks, segments were assigned to lobe subdomains on the basis of standardized landmarks (Fig. 1g, top). A population-level analysis of the apex, flank and mixed subsegments showed no significant difference in anticlinal wall growth rates in these subdomains (Fig. 1g, bottom).

With this imaging pipeline, it was not technically feasible to conduct similar statistical analyses of lobing segments because PDLPs do not provide the spatial resolution needed to analyse the subdomains of emerging lobes, and it was difficult to get a large number of time-lapsed datasets from lobing segments. Nonetheless, we were able to analyse three lobing segments and determine whether their growth behaviours were similar to those of lobed cells. The lobing segments displayed growth heterogeneities that were similar to those of lobed segments (Fig. 1h–k and Extended Data Fig. 1m–o). Interestingly, growth rates in the regions of newly formed lobes varied greatly between segments residing in domains with the highest (Fig. 1k) and lowest (Extended Data Fig. 1n) rates. The warping patterns of lobing segments were variable but not dominated by the locales of lobe initiation (Fig. 1l and Extended Data Fig. 1m–o). These data indicate that polarized growth that generates new lobe features is superimposed on asymmetric growth patterns that occur at the cell segment scale.

To test for a correlation between growth rates and tensile stress, a 3D FE model of the cell clusters was generated using cell geometries obtained directly from the live-cell image data on the cells of interest (Fig. 2a,b and Extended Data Fig. 2j,k). The FE model simulates the cell as a thin-walled pressurized shell with wall properties based on an isotropic, neo-Hookean hyperelastic material behaviour (Methods). On the basis of direct measurements from transmission electron microscopy (TEM) images, the model includes a cell wall thickness of 300 nm for the outer periclinal wall and 40–50 nm for each of the paired anticlinal walls, and it uses experimentally validated turgor pressure measurements and realistic cell wall modulus values on the order of a few hundred MPa (ref. [31]). The model also includes an adherent layer to simulate the middle lamella and independent anticlinal walls in each cell that respond to tensile forces (Fig. 2b). The 3D model generates quantitative predictions of cell wall stress magnitude and direction as a function of location in the cell.

Because of their large size, many cell pairs of interest were not completely captured in the image field. The technical issue of effects of partial cell volumes on stress distributions was addressed in a series of sensitivity analyses (Extended Data Fig. 2a–e) that showed that anticlinal wall stresses based on partial cells were largely unchanged (<10%) except when the majority of one cell was missing. An FE model of the lobing cell pair in Fig. 1h–l was generated on the basis of the estimated area for the partial cell 1 using the maximum height profile of the real cell (Extended Data Fig. 2f–i), and the estimated area of 692 μm^2 is similar to the mean cell area of 634 μm^2 in cotyledons one day after germination (DAG) (Supplementary Table 2). The maximum principal stress (σ_{max}) profiles for the two opposing anticlinal walls were extracted from the FE model (Fig. 2b). Along the cell segment length, there was a general trend for the magnitude of σ_{max} to decrease approaching three-way junctions (Fig. 2b,c and Extended Data Fig. 2k–o), and the shapes of the profiles were most consistent near the top of the wall because stress decreased at increasing depths away from the junction with the periclinal wall (Extended Data Fig. 2e). Because our subsequent analyses focus on the interface of the outer periclinal and anticlinal walls, we report σ_{max} profiles as the average values from the upper eighth of the anticlinal wall.

As expected, σ_{max} tended to be oriented perpendicular to the outer periclinal wall; however, off-axis tensors were frequently observed near the three-way junction and in some regions of high cell curvature (Fig. 2d,e and Extended Data Fig. 2l–o). The vertical component of σ_{max} is not the primary driver of anticlinal wall expansion, since cell growth occurs primarily in the plane of the leaf, probably reflecting the expected cellulose-dependent anisotropy of the anticlinal wall[13]. As σ_{max} deviated increasingly from vertical, the horizontal component (σ_H) of this tensor increased (Fig. 2d–f and Extended Data Fig. 2l–o). Interestingly, within each of the five FE model segments for which σ_H profiles were generated, σ_H correlated with the subsegment growth rates measured using PDLP3 (Fig. 2f and Extended Data Fig. 2l–o). This suggests that the direction of σ_{max} is a key determinant of local growth rates and that within a segment the anticlinal wall is highly anisotropic but has similar material properties along its length. There may be variability in wall material properties between segments, as the growth

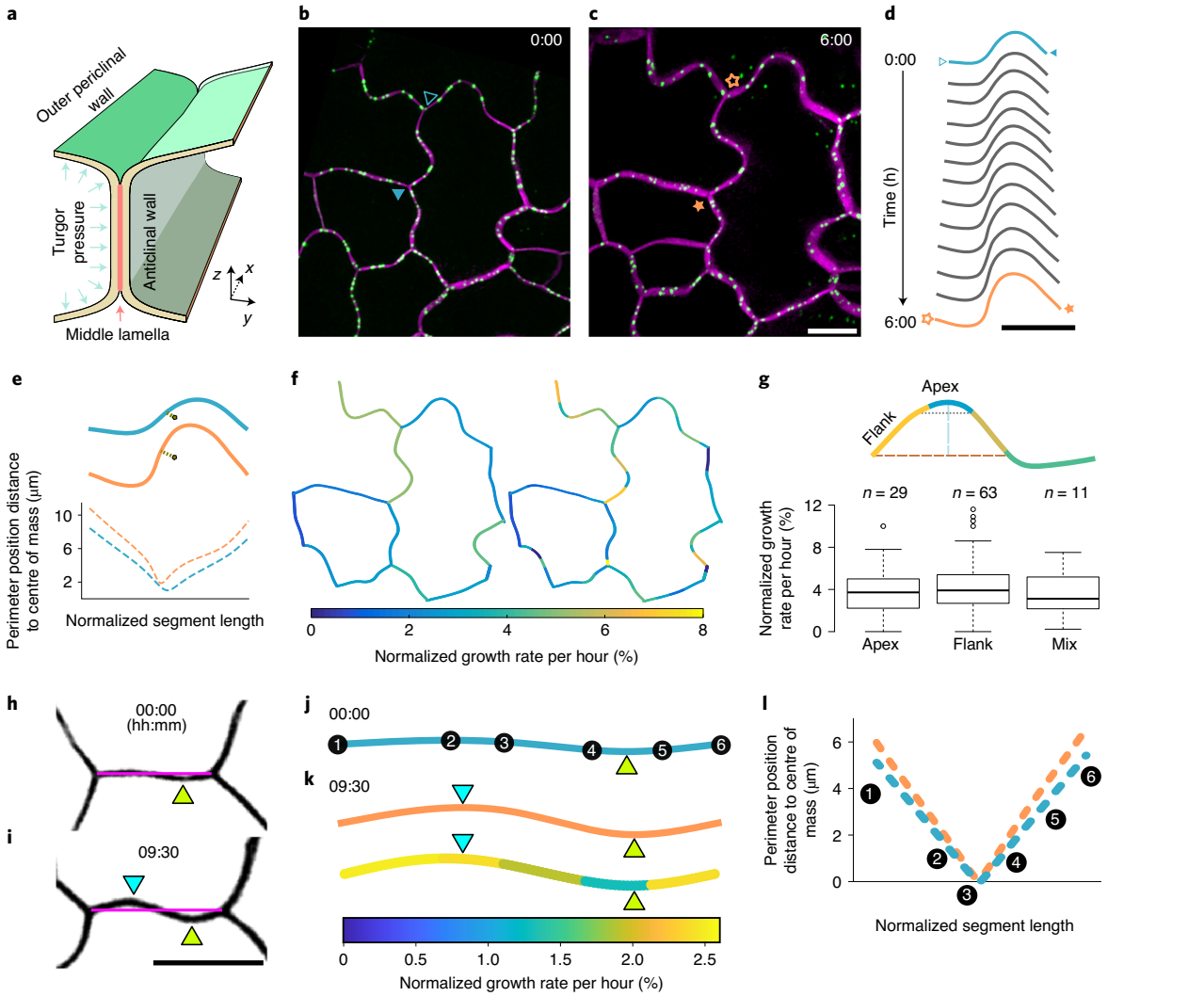

Fig. 1 | Heterogeneous growth of the cell boundary in developing pavement cells. a, Cross-section of the cell–cell interface and nomenclature. **b**,**c**, Example pavement cell field snapshots with tagged plasma membrane (PIP2–mCherry, magenta) and plasmodesmata fiducial marks (PDLP3–GFP, green), 6 h interval. **d**, Segment shape change over time from **b** (blue segment) to **c** (orange segment). **e**, Segment warping analysis using distance along the segment length to its centre of mass after growth (top), which identifies regions of local deformation (bottom). **f**, Spatially mapped growth rates among cell segments in a field (left) and within PDLP-marked subsegments (right). **g**, Lobe geometry does not predict subsegment growth rates. The box plots show the mean growth rates of a population of subsegments with apex, flank or mixed localizations. The centre lines show the medians, the box limits indicate the 25th and 75th percentiles as determined by R software, the whiskers extend 1.5 times the interquartile range from the 25th and 75th percentiles, and outliers are represented by dots. **h**,**i**, Snapshots of a lobing segment 22 min before lobe formation (**h**) and 9:30 h after lobe detection (**i**). **j**, Normalized segment length and shape before lobe formation with PDLP positions marked along the segment. **k**, Top, normalized segment length and shape at the final time point showing the previously existing (green arrowhead) and newly formed (cyan arrowhead) lobes. Bottom, same as top but showing normalized subsegment growth rates. **l**, Warping analysis of the cell segment during lobe formation. The perimeter position distance to the centre of mass is plotted for segment shape at lobe detection (**h**,**j**, cyan) and final segment shape (**i**,**k**, green). PDLPs for the initial time points are mapped onto the warping analysis plot. Scale bars in **c**,**d**,**i**, 10 µm.

rates between segments differed greatly even though simulated σ_H values were similar. These modelling and growth kinematics depict a general planar cell expansion mechanism in which σ_H defines anticlinal wall growth rates, and material properties are maintained via coordinated cell expansion and new wall synthesis. Lobe initiation occurs within this cellular-scale biomechanical context, and the next major challenge was to determine what gene activities and molecular functions control lobe formation.

The central importance of the microtubule–cellulose system during lobe initiation. An initial model for lobe patterning was based on subcellular gradients of auxin and trans-cellular Rho-of-plants small GTPase signalling[14]. However, recent genetic and localization studies failed to detect a pavement cell function for the major components of this auxin-based pathway[12,13]. Given the divergent models proposed for lobe formation and the recently proposed central roles of pectin[17,18], we screened a wide collection of morphology mutants and inhibitors for lobe number defects. Fully expanded wild-type pavement cells have a low area-to-perimeter ratio with a mean circularity value of 0.26 and a mean lobe number per cell of 16 (Supplementary Table 1 and Extended Data Fig. 3a). The *anisotropic1* (*any1*) mutation is in a *CELLULOSE SYNTHASE1* complex subunit and causes defects in microfibril organization and polarized growth[31]. *Any1* had a much simpler overall shape and a reduced

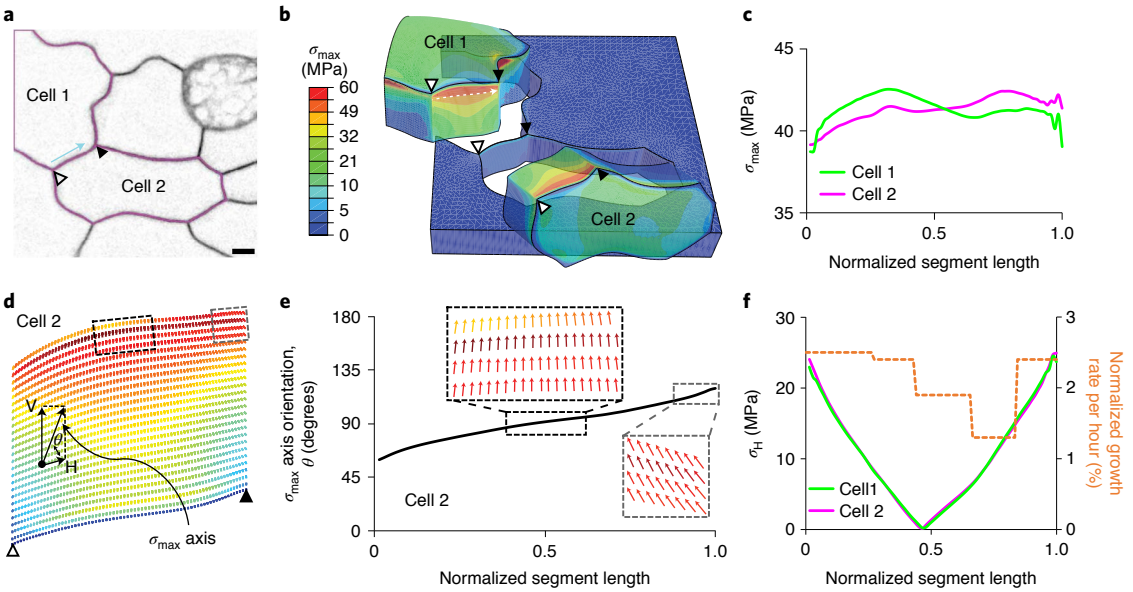

Fig. 2 | Tensile force orientation correlates with subcellular growth rates. a, Cell field used to create the FE model of a pavement cell cluster. The arrow indicates the segment used to compare strain and wall tensile stress patterns. Scale bar, 5 µm. **b**, FE model of two cells showing the variation of σ_{max}. **c**, Distribution of σ_{max} in the anticlinal walls. **d**, Orthographic projection of a representative curved lobing segment. The orientation of each short line represents the σ_{max} axis, which can be divided into its horizontal (H) and vertical (V) components. **e**, σ_{max} orientation across the segment. The dotted boxes show the normal view of the anticlinal wall, and the arrows indicate the magnitude and direction of wall stress and orientation. **f**, Correlation analysis of segment strain and the horizontal component of anticlinal wall σ_{max} plotted graphically as a function of cell position. In **a**,**b**,**d**, black arrowheads mark the endpoints and orientation of the wall segment.

lobe number on both a per-cell and cell-area-normalized basis (Supplementary Table 1 and Extended Data Fig. 3f). KATANIN1 is a known microtubule-severing protein and has been proposed to link cell wall tensile force with morphogenesis[32]. The *ktn1* mutant had a simpler shape than the wild type but no detectable reduction in lobe number. Similar results were obtained with the microtubule plus-end binding mutant *clasp* (Supplementary Table 1 and Extended Data Fig. 3b,c). The lack of a lobe initiation phenotype for *clasp* might be due to the radius of curvature of 2.59 ± 0.27 µm (eight cells) at the transition from the outer periclinal wall to the anticlinal wall, which exceeds the radius of curvature threshold of 2.5 µm, below which CLASP-dependent microtubule stabilization operates[33]. These phenotypes could be explained by a defect in the maintenance of lobe outgrowth rather than lobe initiation, similar to what has been shown for the microtubule-binding protein BPP[27]. A possible effect of the microtubule plus-end binding MOR1 on pavement cell shape has been reported[34]. In our assay, the temperature-sensitive *mor1-1* allele had a reduced lobe number when it was shifted to the non-permissive temperature (Supplementary Table 1 and Extended Data Fig. 3h,j). These data are consistent with the proposed importance of microtubules during lobe initiation, but MOR1 is not a useful molecular marker for the specific microtubules that control lobe initiation because its mutation causes global and severe defects in the cortical microtubule network[35]. The *quasimodo2* (*qua2*) mutant has reduced pectin synthesis[36]. Q*ua2* had a reduced cell size and number of lobes per cell but an increased lobe number when normalized to cell area. There was no indication that *qua2* reduced lobe number when cell protrusions at three-way junctions were manually removed to specifically quantify type I lobes[37]; the mean lobe number per area × 1000 was 1.71 ± 0.76 for *qua2* and 1.13 ± 0.28 for similarly sized wild-type cells. Surprisingly, mutation of the exocyst complex subunit *exo84b*, which is involved in targeted secretion, increased lobe number, pointing to additional pathways that limit lobe initiation (Supplementary Table 1 and Extended Data Fig. 3g).

We conducted a series of inhibitor experiments to analyse microtubule, cellulose and pectin systems in the context of lobe initiation (Extended Data Fig. 3k–q and Supplementary Table 2). In the interval from 1 to 2 DAG, wild-type cells generated about five lobes per cell. Treatment with oryzalin (a microtubule-depolymerizing drug) and isoxaben (an inhibitor of CesA) decreased lobe initiation rates significantly but not the cell areal growth rates relative to controls. Treatment with 0.2% pectinase, which selectively degrades homogalacturonan, had no detectable effect on growth or lobe formation (Supplementary Table 2). We show later that this concentration of pectinase had a strong effect on cell–cell adhesion. The lobing defect was due to microtubule-biased directionality of CESA trajectories in the plasma membrane[38], because time-lapse imaging of YFP–CesA6 and mCherry–TuA5 showed that many linear CESA tracks mirrored the spatial distribution of microtubules (Extended Data Fig. 3r–t). High spatial and temporal time-lapses of CesA and microtubules at the anticlinal wall are not possible due to photobleaching. Resliced snapshots showing the face-on view of the anticlinal wall showed evidence of microtubule–CesA colocalization that was consistent at this location (Extended Data Fig. 3u, right panels). The *csi1* mutant was tested for lobe defects on the basis of its known involvement in coupling CESA to cortical microtubules[39]. Surprisingly, there was no phenotypic difference between *csi1* and wild-type populations (Supplementary Table 1 and Extended Data Fig. 3e). This result reflects the fact that the colocalization of CESA and microtubules was retained at both the outer periclinal and anticlinal walls in *csi1* (Extended Data Fig. 3v–y) and probably involves additional pathways or CSI1-like genes. Collectively, these data suggest that microtubule-dependent patterning of cellulose fibres in the wall is an essential activity to pattern interdigitated growth.

Transfacial microtubules predict the location and direction of lobe formation. High-resolution imaging of the plasma membrane and microtubules consistently detected perpendicular anticlinal

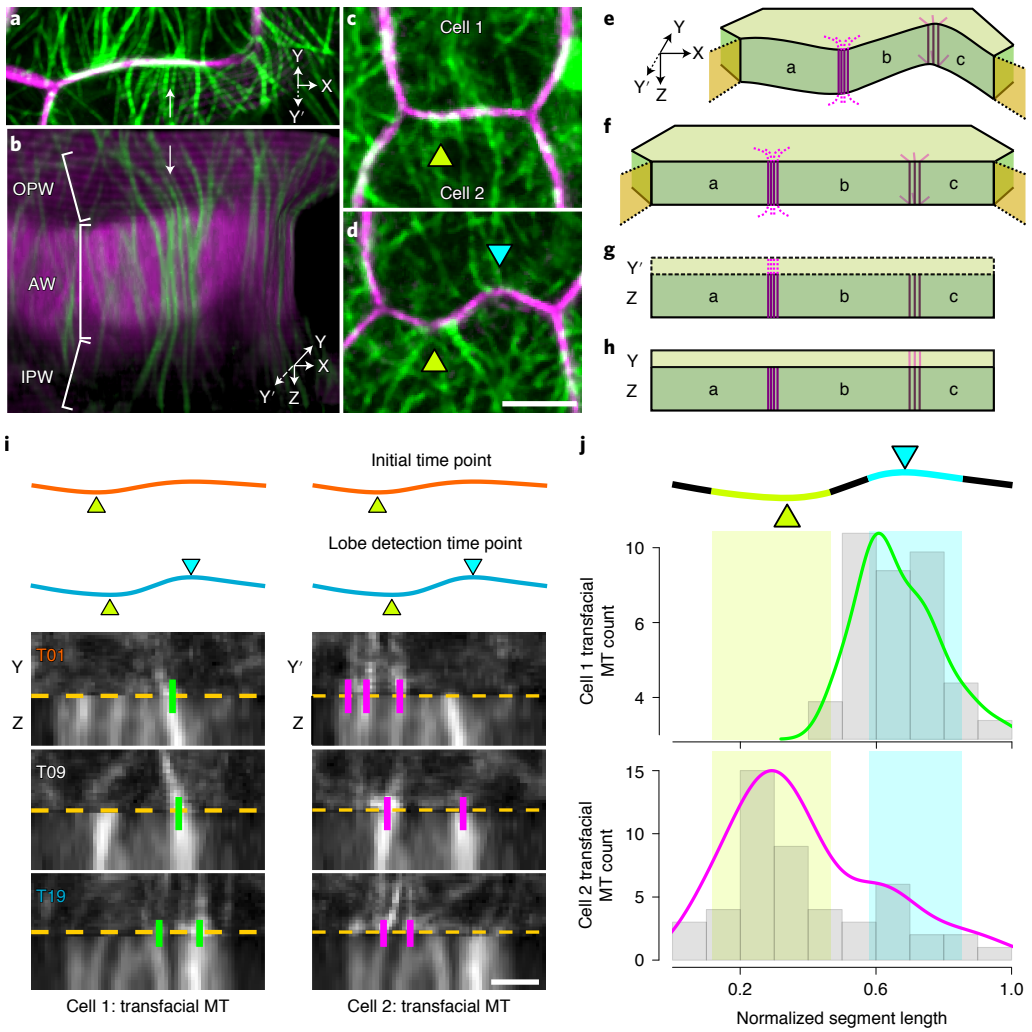

Fig. 3 | Transfacial microtubules predict lobe initiation sites. a, Top view of a segment that will form a lobe; the plasma membrane (magenta) and microtubules (green) are rendered in 3D. **b**, Microtubules (MT) are seen splayed from the anticlinal wall (AW) to the inner and outer periclinal walls (IPW and OPW). In **a**,**b**, white arrows mark the same microtubules in two different views. **c**,**d**, Initial (**c**) and final (**d**) snapshots of a segment that contains an existing (green arrowhead) and a newly formed lobe (cyan arrowhead). **e**–**h**, Method for transfacial microtubule analysis (see Methods for the details) resulting in an image montage of the anticlinal and outer periclinal walls for the adherent cells (**g**,**h**); a, b and c indicate subregions of the coupled anticlinal walls; Y′ indicates the periclinal wall of cell 2; and Y indicates the periclinal wall of cell 1. **i**, Transfacial microtubules at a lobing interface in cell 1 (left) and cell 2 (right). Lobing segment shape (top) at the initial (orange) and lobe detection (cyan) time points. Montaged images of anticlinal and outer periclinal walls at the three indicated time points are shown, with transfacial microtubules indicated with vertical bars (green indicates cell 1; magenta indicates cell 2). **j**, Histograms of transfacial microtubule locations before lobe detection showing enrichment in cell 1 near the lobing region (cyan) and cell 2 (yellow) near the region of an existing lobe. Scale bars, 5 µm for **c**,**d** and 2 µm for **i**.

microtubule bundles that splayed along the cortex of the outer and inner periclinal cell surfaces (Fig. 3a,b). This suggested that microtubules function symmetrically at both periclinal cell surfaces. Time-lapsed analyses of anticlinal wall tilt showed that the anticlinal wall remained straight during lobe formation and outgrowth (Extended Data Fig. 3z–e′) and reflected symmetrical growth of the outer and inner periclinal walls.

To determine how microtubules control lobe formation, we took a multivariate long-term live-cell imaging approach using cells in which microtubules and the plasma membrane were marked (Supplementary Video 2). Prior analyses of microtubules and lobing segments were based on either snapshots of already lobed cells[9,10] or time-lapsed analyses at time intervals of 1 h or greater[13] to 6 h (refs. [15,17]), which is not sufficient because lobe initiation occurs at timescales of tens of minutes (Fig. 3c,d and Supplementary Video 3). Correlation analyses of time-series microtubule imaging consistently showed that the microtubule network turned over in approximately 10 min (Extended Data Fig. 4a–f). Therefore, because of bleaching trade-offs, we selected 10 min intervals, and at this sampling frequency, 32% of all transfacial microtubules were detected in two or more consecutive time points. In this paper, the term ‘microtubule’ refers to either single microtubules or microtubule bundles.

To graph outer periclinal and anticlinal microtubule behaviours as a function of the location and timing of lobe detection, candidate cell segments were tested for lobe formation events post-acquisition using the prominence method[13]. Opposing patches of the outer periclinal cell cortex at the future site of lobe detection do not differ in microtubule density[13]. We found that the orientation and coherency of microtubules in the opposing outer periclinal cell patches also varied wildly as a function of time prior to lobe initiation (Extended Data Fig. 4g–n). This is not unexpected, because many periclinal

microtubules are randomly oriented and enter and exit the region of interest (ROI) from any direction. Despite the high variability of the microtubule network, summed projections of the time-series data consistently revealed hot spots of microtubule signal near the future site of lobe initiation (Fig. 4b and Extended Data Fig. 5p,t).

Transfacial microtubules that span the anticlinal and periclinal walls are strong candidates to control lobe initiation because they can locally define cell wall properties across both cell faces[11]. To quantify transfacial microtubules, 3D images of the lobing interface were straightened, and the outer periclinal walls of the future convex and future concave cells were rotated and aligned with resliced images of the anticlinal surfaces to create a 2D projection of the two faces of each cell (Fig. 3g,h and Supplementary Video 4). Transfacial microtubules were defined as those that had continuity between the outer periclinal and anticlinal cortex (Fig. 3i, magenta and green tags). The location and frequency of transfacial microtubules in both cells were plotted prior to lobe detection. Segment lengths were normalized between time points to account for growth during the time course (Fig. 3j). The future convex cortical domain was defined as a subsegment equal to the width of the lobe feature at its ½ maximal height centred at the lobe initiation site[13]. Notably, there was an obvious enrichment of transfacials in the future convex cell, with the peak centred near the location where the new lobe would emerge (Fig. 3j). Extended Data Fig. 4o–s summarizes identical manual quantification data for five additional independent lobing events with similar behaviours.

To increase the throughput of our microtubule–cell shape cross-correlation analyses, a semi-automated approach was developed. Because the dominant orientations of anticlinal and transfacial microtubules tend to be parallel and orthogonal to the anticlinal wall (Fig. 3i and Extended Data Fig. 5c,f), a line profile of the summed microtubule intensity in a vertical sector was used to graph microtubule signals on this cell face as well. Microtubule signals were plotted cumulatively over the time course up to the time point prior to lobe initiation (Extended Data Fig. 5g–n). The plots were noisier than the manually scored images because all microtubule signals along the segment were included; however, there was a consistently elevated microtubule signal in the future convex periclinal domain compared with an equivalent region at the future concave domain (Fig. 4c,e and Extended Data Fig. 5n,s,w). In all datasets, there was a large degree of temporal variability in the degree of microtubule enrichment, with the highest values often occurring at a few sequential time points (Fig. 4d). Similar trends in temporal variability were observed in manually scored time-series data (Extended Data Fig. 4t–y).

The mean degree of microtubule enrichment prior to lobe initiation varied greatly among future convex domains (Fig. 4e and Extended Data Fig. 5o), indicating that there is no single microtubule behaviour that is sufficient to predict lobe formation events. However, this microtubule organization has the power to influence cell shape. In one time series, the symmetry-breaking event operated against a clearly existing broad concave bulge (Extended Data Fig. 5x–a′). This asymmetric and localized lobe initiation event cannot be explained by a buckling event as previously claimed[17]. These analyses demonstrate that transfacial microtubules persistently accumulate at a cortical site that accurately predicts the location and direction of lobe initiation.

Cell wall tensile forces predict locations of microtubule enrichment. The mechanism that determines the spatial pattern of cellular interdigitation is not known. Lobe formation conforms to a minimum spacing rule[37,40], and in our time-lapse analyses, lobes never formed within an existing lobe and tended to appear at the midpoint of straight regions of the anticlinal wall that were greater than 6 µm. Biomechanically, it is possible that this geometric bias reflects local regions of elevated cell wall tensile force. Prior FE modelling and microtubule imaging showed that microtubule orientation can mirror cell wall stress[20], and our FE simulations of a lobing segment indicated that σ_{max} profiles can differ between adjacent anticlinal cell walls (Fig. 2c).

To determine whether patterns of cell wall tensile forces correlated with microtubule behaviours that relate to lobe initiation, a 3D model was created on the basis of image data on lobing cells (Fig. 4f–h). As expected in lobing segments[13], cortical microtubules along the anticlinal walls were highly oriented parallel to σ_{max} tensors (Extended Data Fig. 5a–f). The spatial distributions of σ_{max} values were quantified in the upper eighth of the anticlinal (Fig. 4i) and outer periclinal (Fig. 4j) walls adjacent to the cell–cell junction. The stresses along the anticlinal wall were around 120 MPa, and cell 1 had a small peak of anticlinal wall stress centred at the future convex region of the cell (Fig. 4i). The sectors of the two adjacent periclinal walls along the cell segment had a more offset pattern of stress. In cell 2, the stress maximum correlated with the convex curvature of an existing lobe (Fig. 4j). Cell 1 had a peak of slightly elevated stress that was centred near the future lobe location. FE models were constructed for two additional lobing segments, and the same pattern held. Stress profiles were similar along the anticlinal wall, and the future convex cell had a locally elevated tensile force in the periclinal wall that was at or near the future convex cortical domain and the site for microtubule enrichment (Extended Data Fig. 5r,s,v,w). The stress predictions of the model are approximations of the real cell behaviour because cell wall properties were assumed to be homogeneous, but these analyses were consistent with tensile force acting as an upstream patterning element during interdigitated growth. In this scenario, microtubules convert tissue-scale and cellular-scale tensile force patterns into a polarized growth process that leads to lobe formation.

A cell-autonomous system to analyse wall stress, microtubules and lobing. We next used cell–cell adhesion mutants and pectinase treatment to decrease cell–cell adhesion and enable cell-autonomous growth to generate cells with altered shapes and tensile stress distributions. If the future convex cell uses the microtubule–cellulose systems to initiate lobe formation, then a central function of pectin and the middle lamella could be to mechanically couple the initiating cell with complementary polarized growth in the following cell. We had noticed previously that the cell–cell adhesion mutant *qua2* had unusual invaginations at the cell periphery (Fig. 5a). We wanted to examine the ultrastructure of furrows using electron microscopy, but *qua2* seedlings were too fragile to survive the sample processing protocol. As an alternative, we turned to the known cell–cell adhesion mutant *dis2* (ref. [41]), which also occasionally displayed clear invaginations at the cell periphery (Fig. 5b,c). Invaginations were not observed in wild-type control samples that were not pectinase-treated (Fig. 5d). In medial longitudinal thin sections through *dis2* furrows, closely opposed cell walls from the same cell and a widened bulb at the apex were observed (Fig. 5e). The apex was frequently enriched with cortical microtubules that could be seen in the cross-section. This cell geometry, microtubule organization and ultrastructure exactly matched the invaginations that have been detected in lobed mesophyll cells[42]. Furthermore, a previous analysis of cell–cell adhesion in the context of organ development included a time-lapse image series documenting the slow inward progression of a furrow-like structure[43]. Furrows are generated over timescales of hours and reflect a shape deformation that is generated by slow, irreversible and highly anisotropic growth.

The progressive invaginations of pectinase-induced furrows were generated by microtubule- and cellulose-dependent processes, because the delaminations and furrows were greatly reduced by oryzalin and isoxaben at concentrations that did not inhibit cell expansion (Fig. 5f). The similar growth patterns and inhibitor sensitivities of furrows and lobe formation during normal cotyledon

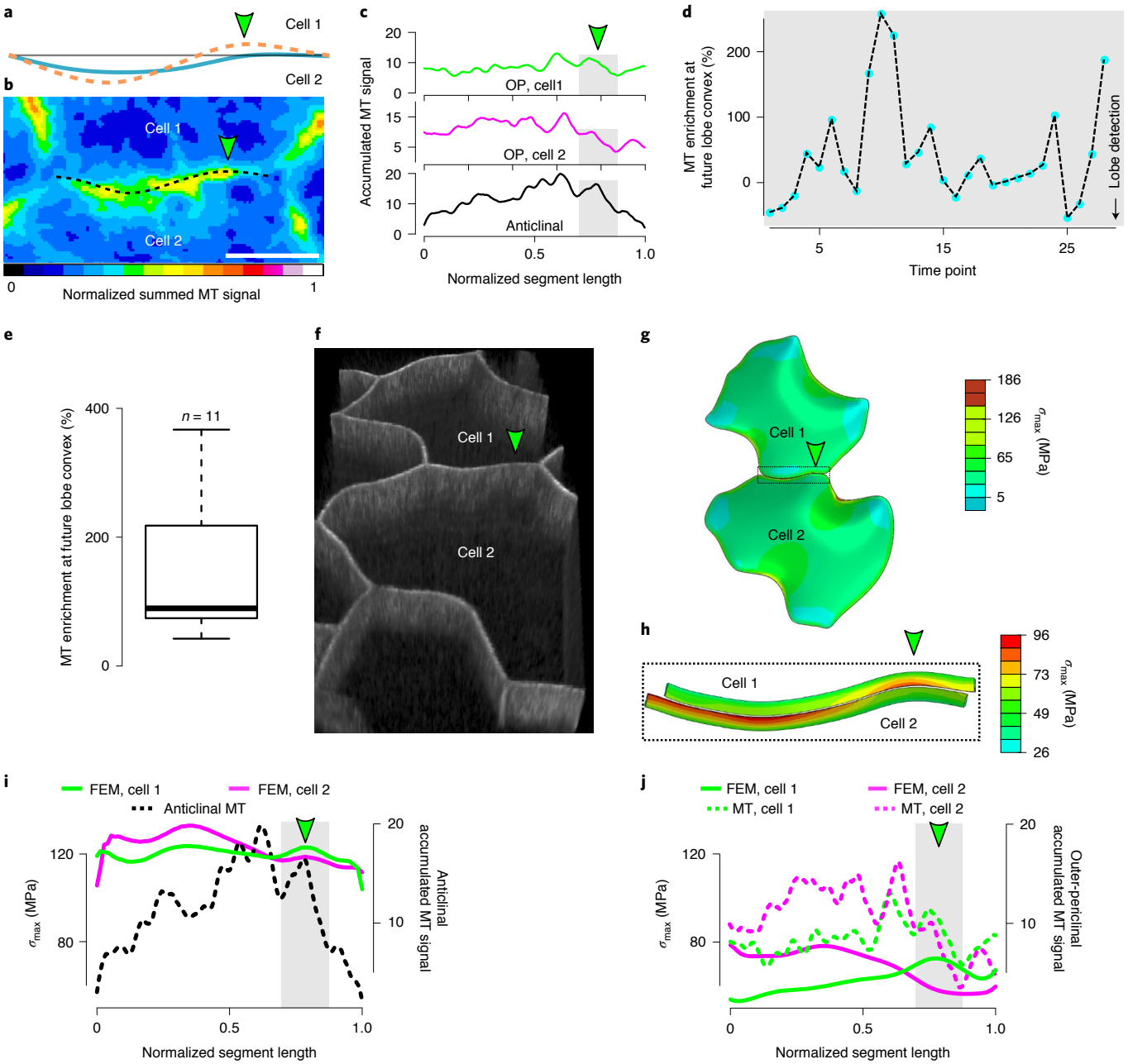

Fig. 4 | Microtubule signals are concentrated at regions of elevated cell wall tensile stress. a, Segment shape at the start of the time-lapse (blue) and at the time point of lobe detection (dashed orange) that is used for the analysis in **c**,**d**,**f**–**j**. The green arrowhead denotes the location of the new lobe. **b**, A heat map of normalized microtubule signal intensity before lobe initiation shows a hot spot at the future lobe initiation site (green arrowhead). Scale bar, 5 µm. **c**, Accumulated microtubule signal intensity at the periclinal cortex (OP) of cell 1 (green line), cell 2 (magenta line) and the anticlinal cortex (black line) before the lobe is detected. The future lobe site is the region shaded in grey. **d**, Plot of microtubule enrichment at the future convex side of the new lobe over time. Enrichment $= 1 - \frac{\text{Area under curve}_{\text{Cell1}}}{\text{Area under curve}_{\text{Cell2}}} \times 100$. **e**, Box plot of microtubule enrichment at the future lobe convex before lobe detection. The centre line shows the median, the box limits indicate the 25th and 75th percentiles as determined by R software, the whiskers extend 1.5 times the interquartile range from the 25th and 75th percentiles, and *n* is the number of lobing segments analysed. **f**,**g**, 3D rendering (**f**) of the cell pair used to construct the FE model shown in **g** before the new lobe was detected (the green arrowhead is the future lobe region). **h**, Zoomed-in view of the segment from **g** (dotted rectangle) with σ_{max} gradients mapped on the outer periclinal walls adjacent to the anticlinal walls. **i**, The accumulated anticlinal microtubule signals before lobe detection (dashed line) and anticlinal wall stress distributions from cell 1 (green) and cell 2 (magenta) from the finite element model (FEM) are plotted as functions of normalized segment length. **j**, The accumulated periclinal microtubule signals (dashed lines) and periclinal wall stress distributions (solid lines) for cell 1 (green) and cell 2 (magenta) are plotted as functions of normalized segment length.

development (Supplementary Table 2) indicate that these two morphogenetic processes employed similar cell shape control mechanisms. Interestingly, bidirectional furrows were occasionally observed (Fig. 5c), indicating that at least in some instances, the directionality of the invagination is not predetermined by existing cell wall material properties at the time of pectinase treatment.

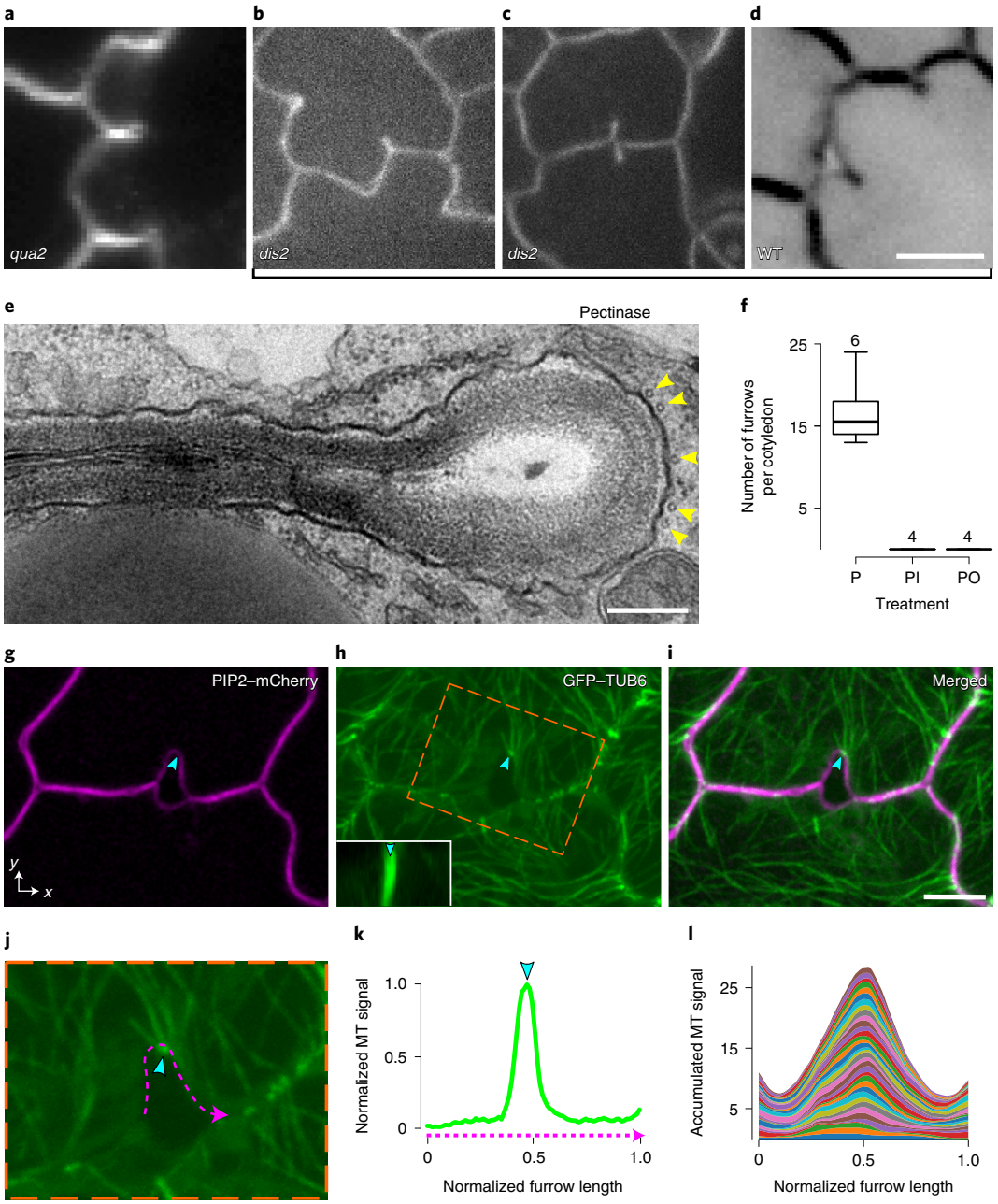

Fig. 5 | A system for inducible cell-autonomous lobing. a, The pectin-deficient mutant, *qua2-1*, develops cell invaginations in pavement cells. **b**,**c**, Pavement cell furrows in the cell–cell adhesion mutant *dis2*. **d**, Furrow formation induced in the wild type by 0.2% pectinase treatment. **e**, TEM analysis of an induced furrow in *dis2*. The arrowheads indicate cortical microtubules. **f**, Box plots of the number of furrows per cotyledon of wild-type, pectinase-treated seedlings. P, pectinase; O, oryzalin; I, isoxaben, at 0.2%, 1 nM and 5 µM concentration, respectively. The centre lines show the medians, the box limits indicate the 25th and 75th percentiles as determined by R software, and the whiskers extend 1.5 times the interquartile range from the 25th and 75th percentiles. The number above each box plot is the number of cotyledons analysed. **g**, Face-on view of a nascent furrow developing from pectinase-induced delamination. **h**,**i**, Splayed microtubules at the apex of a nascent furrow. **j**, Inset region of **h**. The furrow is outlined in magenta, and the microtubule signal maximum is shown with a cyan arrowhead. **k**, Plot of normalized furrow position and microtubule signal to enable a population-level analysis. **l**, Population-level analysis of microtubule signals and locations along nascent furrows ($n = 36$). Panels **g**–**l** were generated using wild-type pectinase-treated cells. Scale bars, 10 µm for **a**–**d**, 250 nm for **e** and 5 µm for **g**–**i**.

To analyse microtubule localization in furrows more quantitatively, we identified rare early-stage invaginations in which an asymmetrically expanded feature was present at the site of pectinase-induced delamination. In nascent furrows, the delamination was not symmetrical, one cell boundary was more invaginated than its neighbour, the opposing cell walls were not appressed and there was no terminal bulb (Fig. 5g). Similar to convex sites of lobing pavement cells, the curved apex of the nascent furrows frequently had anticlinal microtubule bundles that splayed out at the anticlinal/periclinal wall interface (Fig. 5h,i). When line scans of microtubule signal intensity were plotted as a function of position along the plasma membrane boundary for a population of nascent

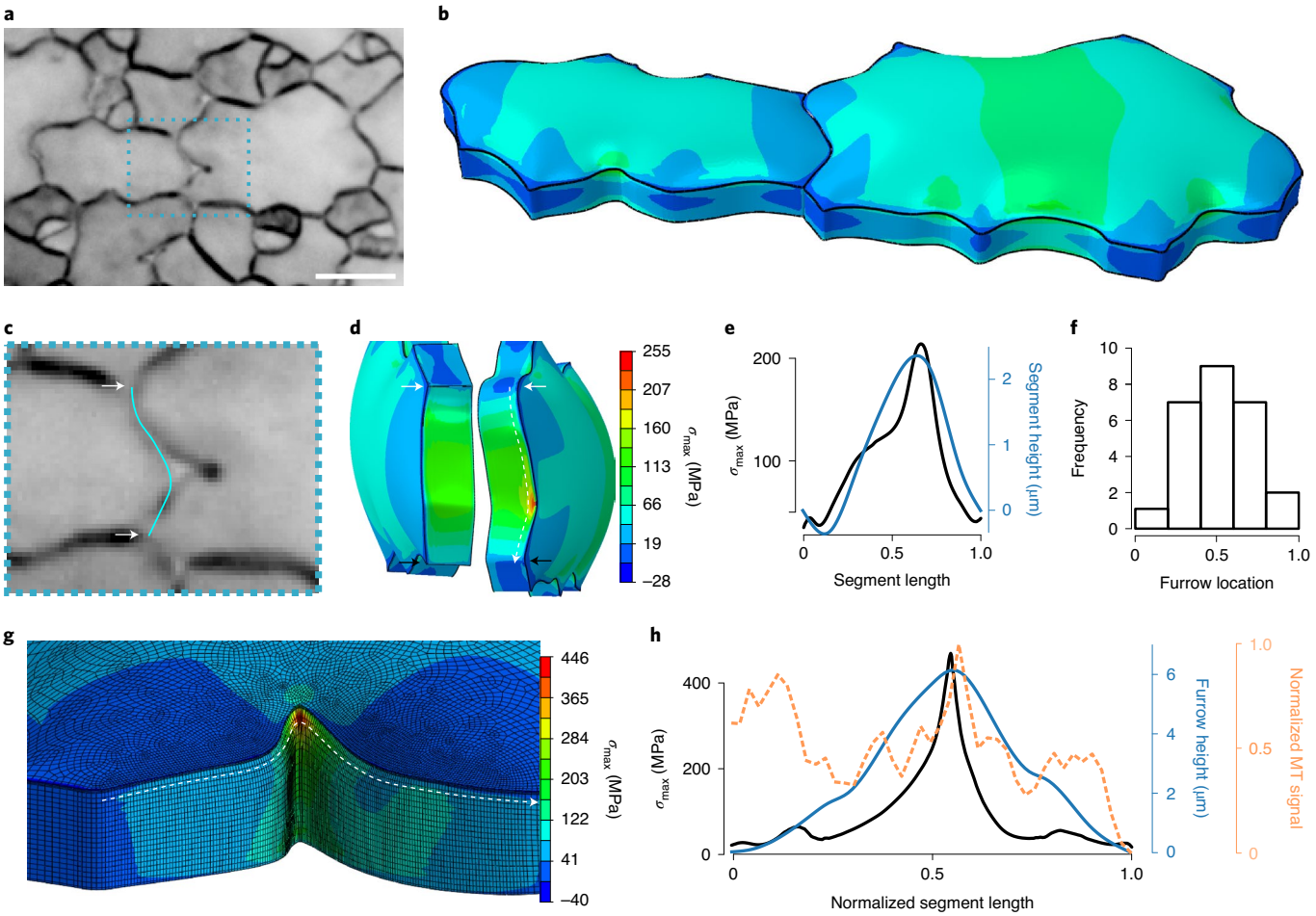

Fig. 6 | Cell wall stress dictates the location and direction of furrow formation. a, Face-on view of pectinase-treated cells displaying furrows. Scale bar, 10 μm. **b**,**c**, An FE model of the estimated shape of the cell pair before furrow formation (**b**) using the flanking cell contours shown in **c**. **d**, Visualization of the anticlinal wall stress patterns of the furrowing cell (right) and its neighbour (left). **e**, Line plot of anticlinal wall stress and segment height relative to a baseline connecting the three-way junctions. **f**, Population-level analysis of furrow location and normalized distance along the segment. **g**, Heat map of cell wall stress of the furrowed cell in **a**. **h**, Aligned peaks of cell wall stress (black line in **g**), microtubule signal (orange) and segment shape (blue) in a furrow.

furrows, there was a strong bias towards location at the apex (Fig. 5j–l). This bias in the more polarized cell at delamination probably reflects the microtubule-dependent generation of the asymmetric cell shape, which perhaps includes the focusing of tensile force that could provide positive feedback on microtubules during invagination (see below). This cell-autonomous lobe/furrow formation system demonstrates the existence of an initiating cell that uses the microtubule and cellulose systems to drive cell ingrowth. The pectinase-sensitive middle lamella couples that asymmetric growth to the adjacent cell.

Cell wall tensile force patterns define the location and pattern of furrow formation. If furrow formation parallels interdigitated growth, then cell wall tensile stress patterns should influence their patterning and development. Pectinase treatment provided a highly useful experimental manipulation that enabled cells to delaminate in response to endogenous cell wall stress patterns and generate unique cell shapes with altered stress distributions. FE modelling was used to analyse both of these processes by constructing a model based on the image data of a cell pair with a nascent furrow (Fig. 6a). We found that furrow location was strongly biased to the mid-region of the segments (Fig. 6f), similar to initiating lobes. In the furrowing cell pair, the location and directionality of the furrow corresponded to the stress maximum of the future convex cell when the FE model boundary was approximated to follow the interpolated pre-furrow shape (Fig. 6b–e). To test for spatial correlations between wall tensile stress and microtubule localization, another FE model was constructed that followed the observed contour of the nascent furrow (Fig. 6g). A very focused stress maximum of ~440 MPa was centred on the furrow apex at the junction of the outer periclinal and anticlinal walls. The high stress is due in part to the local high curvature at the apex, and this location also corresponded to the largest anticlinal microtubule peak along the entire segment (Fig. 6h). The biomechanics and cellular mechanisms of cell-autonomous furrow formation are therefore indistinguishable from those of interdigitating pavement cells.

To evaluate the potency of a microtubule-patterned cellulose-rich patch for cell shape change, an FE model was constructed on the basis of a lobing cell pair with a 2-μm-wide anisotropic patch that mirrored the directional stiffness of cellulose fibres and spanned the anticlinal and outer periclinal walls (Extended Data Fig. 6a–e). After a single iteration of wall loading and relaxation, the anisotropic patch locally distorted the cell–cell interface to form a distinct convex feature compared with the isotropic control cell (Extended Data Fig. 6f,g). The anisotropic patch-dependent deformation was more than 200 nm above that of the isotropic model, which is similar

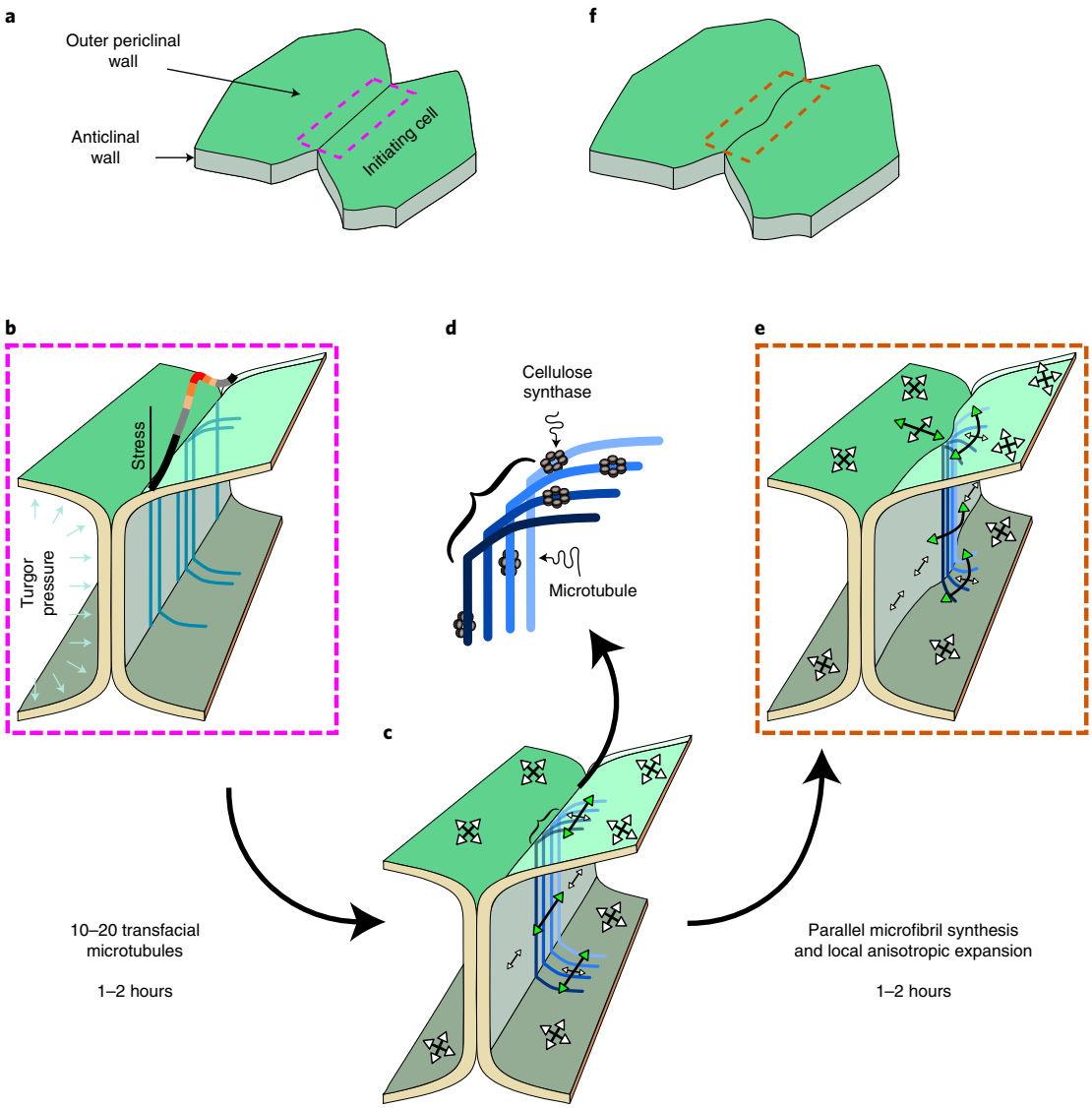

Fig. 7 | A general model for lobe morphogenesis and interdigitated growth. a, An example cell segment before lobe formation. **b**, Inset of **a**. Tensile stress is slightly elevated in the initiating cell due to geometric and wall composition variables. **c**, Microtubules are locally stabilized in response to the stress gradient. **d**, CESA complex motility in the plasma membrane is defined by local microtubule orientation, generating a small patch of the cell wall with anisotropic character. **e**, The initiating cells grow anisotropically in the region of the fibre-reinforced patch, and cell–cell adhesion and anisotropic expansion of the following cell in the direction of the anticlinal wall causes symmetry breaking. **f**, A recognizable new lobe is formed.

to the magnitude of stable features that were detected in time-lapse light microscopy experiments. This simulation demonstrates the ability of a microtubule-patterned cell wall heterogeneity at the micron scale to program a tissue-scale symmetry-breaking event.

Discussion

Multiscale growth control. A major challenge in biology is to understand how the cytoplasm patterns the polarized growth of groups of cells to generate a tissue with specialized functions. Interdigitated growth in the leaf epidermis controls the expansion of thin, durable leaves[3,7]. Here, we used the *Arabidopsis* cotyledon development system to discover how cell wall tensile force and a specialized population of microtubules initiate interdigitated growth (Fig. 7). Lobe formation is first detected as a local nanoscale ~300 nm warping[13] that is driven by microtubule-programmed and cellulose-microfibril-programmed anisotropy in a small patch of wall in an initiating cell. These tiny features have a multiscale influence on morphogenesis because they become stabilized, and slow, irreversible growth over a period of days morphs the feature into a well-defined lobe with features at ~10–50 µm scales[19,21,27]. This work defines the mechanism, timeline and type of cell wall patterning that serves as a general model for polarized diffuse growth and provides a foundation to analyse epidermal morphogenesis across wide spatial scales. The proposed anisotropic growth-based mechanism was previously outlined[11] and bears no resemblance to the varied iterations of growth-restriction ideas in which a local increase in wall thickness, cellulose synthesis or stiffened pectin are proposed to locally inhibit cell expansion and cause lobe formation at some adjacent region[9,10,17,29,44–48]. The initiating cell/anisotropic cell-wall-patch mode of lobe formation is supported by an FE model, which includes anisotropic material properties (Extended Data Fig. 6). Although the proposed cellulose-rich patch of cell wall may be relatively stiff, it permits cell expansion perpendicular to the orientation of the fibres, and the resulting growth parallel to

the anticlinal–periclinal cell wall boundary can drive symmetry breaking (Fig. 7c–f).

The morphological potency of localized transfacial microtubules. Central to this conserved mode of tissue morphogenesis is a morphologically potent subset of transfacial microtubules (Figs. 3 and 7c–e and Extended Data Fig. 4). Prior live cell studies on lobe formation did not analyse plasma-membrane and microtubule markers at a temporal resolution that would allow lobe initiation or the relevant microtubules to be detected[13,15,17]. Our multivariate live cell imaging pipeline captured microtubule organization and cell boundary changes along both the anticlinal and periclinal walls at 10 min intervals for 3.5 to 8 h. This enabled us to detect and quantify the strong enrichment of transfacial microtubules at cortical sites that would later generate lobes.

The central importance of the microtubule–cellulose system was supported by a series of mutant analyses and inhibitor studies. Only the mutation of *MOR1*, an essential microtubule-associated protein[35], and *any1*/*cesa1* had clearly reduced lobe number phenotypes (Supplementary Table 1). Other mutants affected lobe outgrowth or cell size, which are often misclassified as lobe initiation mutants on the basis of manual lobe calls or dimensionless shape descriptors such as circularity. Inhibitor studies also showed that compounds that disrupt microtubules and cellulose synthesis reduced lobe initiation, while pectinase treatment did not (Supplementary Table 2). Historically, microtubules have figured prominently in growth-restriction models of lobe initiation[9,14], and more recently, additional pectin-based models for lobe initiation control have emerged[17,18]. The case for pectin-mediated lobe formation is weakened by the lack of a known mutant in pectin biosynthesis or modification that has a clear reduction in lobe number. In our assays, pectin mutants and pectinase treatment had the strongest effect on cell size, not lobe initiation. This phenotype probably reflects critical functions for pectin as the major matrix component of the wall that affects microfibril–microfibril interactions and cell wall stiffness. Short-term pectinase treatment did not significantly reduce cell size (Supplementary Table 2), and the clearest effect of *qua2* and pectinase treatment was to promote delamination and enable highly polarized cell-autonomous lobing (Figs. 5 and 6 and Supplementary Tables 1 and 2). This pectinase-induced invaginating growth required a functional microtubule–cellulose system (Fig. 5f) and was mechanistically identical to the lobing of adherent cells (Figs. 5 and 6). The simplest explanation is that pectin has secondary functions during lobe initiation, by promoting cell–cell adhesion and perhaps affecting the local modulus of initiating and/or following cells to enable lobe expansion.

The net vertical alignment of the microtubule is a stable feature of the anticlinal cell face of pavement cells (Extended Data Fig. 5c,f and Belteton et al.[13]). We propose that the combination of increased thickness of the outer periclinal wall and the high degree of cellulose-encoded anisotropy in the anticlinal wall restricts increases in cell height and promotes expansion in the plane of the leaf surface. This organization seems to enable the horizontal component of tensile stress in the anticlinal wall to locally dictate growth rates (Fig. 2f and Extended Data Fig. 2l–o). Given that σ_H is on the order of 10 MPa acting on an anticlinal wall with a thickness of ~30 nm and a height of ~10 µm, it is estimated that a force of ~3 µN is needed to drive lateral expansion and increase the distance between oriented microfibrils. Highly aligned microfibrils are also present in the anticlinal walls of epidermal cells of maize coleoptiles[49], and it is possible that this cell-face-specific microtubule–microfibril system plays a central role at cellular scales to polarize diffuse growth.

Transfacial microtubules have morphogenetic power in the context of lobing because they can efficiently align trajectories of CESA complexes and cellulose microfibrils across adjacent cell faces in a localized cortical domain (Fig. 7c–f). This model is consistent with the equivalent effects of mutations and inhibitors of both microtubules and cellulose synthesis (Supplementary Tables 1 and 2 and Extended Data Fig. 3) and the co-alignment of CESA trajectories and microtubules in lobing pavement cells (Extended Data Fig. 3r–t). Transfacial microtubules program the synthesis of a local patch of anisotropic cell wall. The end result is not growth restriction. Fiducial mark tracking along the anticlinal wall (Fig. 1) and time-lapse analyses showed that lobe apices are actively growing features (Fig. 1g,k and Supplementary Video 3). An anisotropic patch of wall that mirrors fibres aligned along the anticlinal and periclinal surfaces of one cell has been hypothesized to promote anisotropic expansion parallel to the cell boundary and initiate lobe formation[11]. FE simulation reinforces the plausibility of this symmetry-breaking mechanism and indicates that the proposed wall patterning in an initiating cell and the resulting growth behaviours can warp the cell boundary and initiate lobe formation (Extended Data Fig. 6 and Fig. 7f).

Beyond a preferential enrichment of transfacial microtubules in the initiating cell, there was no unique microtubule behaviour associated with lobe initiation. Both the degree and time interval of transfacial microtubule enrichment prior to lobe detection varied greatly among events (Fig. 4e and Extended Data Figs. 4t–y and 5o). This probably reflects the numerous parameters that influence the localization and morphogenetic power of microtubules. What is the nature of the cell wall stress profile along a particular cell–cell interface? How many CESA complexes were recruited during its lifetime? How many microfibrils were synthesized, of what length and with what degree of coupling to the matrix? To what extent does microfibril-dependent CESA alignment locally operate as a positive feedback loop for anisotropic wall patterning[50]? What are the size, position and degree of anisotropy in the cell wall patch? The stiffness of the outer periclinal wall of the adjacent following cell could also strongly affect lobe initiation. Clearly, the notion that increased cell size drives lobe formation is too simplistic[16]. The time-lapse analysis of microtubule-dependent symmetry breaking shows that neither the site of lobe initiation nor its direction is determined solely by cell size or pre-existing convex cell boundary (Extended Data Fig. 5x–z). Furthermore, the lobing outcome is not dictated by pre-existing cell wall properties, because in some instances, bidirectional furrows formed at the same location in both cells (Fig. 5c). Lobe formation is analogous to a tug-of-war between two mechanically coupled cells, in which small differences in tensile force tensors can bias transfacial microtubule occupancy, ultimately dictating the location and direction of lobe formation. Any parameter that affects tensile force locally can influence the polarity of the process. In two time-lapse experiments, there was a well-defined interval of ~2 h during which transfacial microtubules were enriched prior to lobe detection (Extended Data Fig. 4u,y). These results indicate that relatively few (about ten) localized transfacial microtubules can program a detectable morphogenetic output with a time lag of ~1 h.

We emphasize that transfacial microtubules and sensitized growth control at the cell–cell interface may be a general feature of plant cell and tissue morphogenesis. Diffuse growth is assumed to be uniform across the cell surface. However, when densely distributed particles are used as fiducial marks, even in simply shaped hypocotyl epidermal cells, considerable subcellular growth heterogeneity is detected[19]. Hypocotyl cells adopt several distinct microtubule configurations on different cell faces[51], and in general the subset of microtubules and the subcellular patterns of growth that dictate shape change are not known.

Cell wall stress is a multiscale upstream patterning element. Lobing follows a minimum spacing rule[37,40], and the underlying cellular patterning mechanism for lobe formation has been controversial[12–14,52]. A combination of pavement cell FE modelling and microtubule imaging showed examples of subsets of well-defined

lobes in which the patterns of tensile stress and microtubules were similar[17,20]. However, neither quantitative analyses of microtubules and tensile force alignment nor an analysis of associated growth were performed. Microtubule enrichment along the convex surface of a lobe is transient and displayed only at a subset of lobes[13,27], leaving open the question of how cell wall stresses might influence lobe outgrowth. Here we used FE models of pavement cell clusters to simulate the magnitude and direction of cell wall stress patterns quantitatively and test for correlations with microtubule behaviours and lobe initiation. We show that microtubules were correlated with stress in three different ways (Fig. 7b). First, microtubules are depleted at three-way junctions[13], and wall tensile forces are often reduced near the mechanically stabilized three-way cell wall (Figs. 2c, 4g–j and 6d,e and Extended Data Fig. 2). Second, microtubules along the anticlinal walls are highly aligned perpendicular to the leaf surface (Fig. 3b,i and Extended Data Fig. 5c,f; see also Belteton et al.[13]), as are the maximum principal cell wall stresses (Fig. 2e and Extended Data Fig. 5b,e). They also have the potential to globally align the microtubule–microfibril systems along the anticlinal face and influence local microtubule alignment of the outer cell face when subsets polymerize across the cell-face boundary. This proposed control system could promote a planar bias to cell expansion in any epidermal cell type with this organization[49,53], and in pavement cells the directionality and spatial distribution of the stress probably contribute to differential growth rates along the anticlinal segments (Fig. 2f and Extended Data Fig. 2l–o). As σ_H and growth rates are elevated in subsets of lobes (Extended Data Fig. 2m), lobe features and resulting increases in σ_H could enable increased growth rates from cell to organ scales. Third, there were local anticlinal and periclinal wall tensile stress peaks that correlated with the location of transfacial microtubule enrichments and subsequent lobe initiation sites (Fig. 4i,j and Extended Data Fig. 5s,w). These stress profiles are estimates of those that exist in real cells because the wall was treated as a homogeneous material, but nonetheless they consistently point to the ability of the microtubule system to sense subcellular gradients of tensile stress.

Wall stress patterns were strongly altered in pectinase-treated cells with broad delaminations and cell invaginations. In this cell-autonomous lobing system, wall stress maxima predicted the sites of delamination. Delamination was not an elastic response, because it required polarized growth and an intact microtubule–cellulose system (Fig. 5f). Asymmetric delamination had an apical curvature with a highly focused cell wall stress maximum. The strong and consistent concentration of microtubules at the furrow apex and the active invagination of furrows that developed in a microtubule- and cellulose-dependent manner also indicate that local wall stress gradients are sensed to pattern polarized diffuse growth. In the context of an intact tissue, outer periclinal wall tensile forces near the cell boundary tend to be reduced in concave regions and elevated in convex regions and around the mid-regions of extended straight domains (Extended Data Fig. 2k,o; the cyan arrowheads indicate convex regions, and the orange arrowheads indicate concave regions). The coupling of these tensile stress patterns to the microtubule–microfibril system could explain the spacing rules of lobe formation.

Our TEM analysis showed that the morphology and microtubule localization in pectinase-induced furrows (Fig. 5e) were identical to those of highly furrowed leaf mesophyll cells with a terminal bulb[43]. We believe that we have described a general mechanism of lobe formation. In specialized mesophyll cells, this subcellular trait is linked to more efficient CO_2 transport to chloroplasts and has clear importance in crop productivity[54,55]. A key challenge now is to determine how cortical microtubules sense the large and oriented tensile forces in the cell wall without being ripped apart.

Cell wall stresses serve as useful multiscale patterning elements during tissue morphogenesis (Fig. 7). Tensile forces are concentrated at the interface where the unpaired outer periclinal walls pull upwards on anticlinal walls with stresses that reflect cell-autonomous parameters such as cell size and local height. Tissue-level parameters such as the length and local curvature of the shared anticlinal wall also shape subcellular stress gradients that are decoded by the microtubule system. Along the anticlinal wall, the distance from and angles among cell walls at three-way junctions[56] may also affect stress distributions. Stress is sensitive to the material property gradients in the cell wall and varies inversely with cell wall thickness[30]. Wall stress patterns may also reflect the local growth status, because within a pavement cell, growth rates within a segment often vary by factors of 2 to 7 (Fig. 1f and Extended Data Fig. 2j), and wall thickness varies by a factor of ~2.5 (ref. [13]) due to imperfect maintenance of wall thickness during cell expansion. Interestingly, some of the largest microtubule bundles may be localized to the thinnest regions of the anticlinal wall (see Figure S13C in Belteton et al.[13]), and this may reflect a general wall tensile force sensing mechanism that prevents cell rupture. Our analyses indicate that cell wall stress patterns influence microtubule array organization at cellular scales, and the microtubule–cellulose system uses cell wall stress to reliably convert numerous geometric and physical parameters into a patterned morphogenetic response.

The cellular (Fig. 7) and computational FE (Extended Data Fig. 6) models of lobe initiation are derived from mutant phenotypes, high-resolution multidimensional imaging and quantitative determinations of the geometry and type of cell wall anisotropy that can cause lobe formation. The model is certainly imperfect, as it includes only a small subset of the cell wall heterogeneities and tissue-scale forces that operate in vivo; however, it is based on realistic values for cell wall thickness, modulus and turgor pressure[31]. In another pair of FE modelling and imaging-based papers, a pectin-mediated patchwork of periclinal wall stiffening and predicted compression forces in the anticlinal wall were proposed to cause lobe initiation. The two-step mechanism invokes microtubules and cellulose only to reinforce an already established polarity[17]. The FE stiffness inhomogeneity model[29] of lobe initiation requires a highly defined patchwork of outer periclinal wall domains with differing stiffnesses, a condition that has not been clearly demonstrated in vivo[17]. The stiffness inhomogeneity FE simulations point to the importance of compression forces in the anticlinal wall to cause lobing[29], something we have not observed in any of our 3D FE cell cluster models. Perhaps the failure to pressurize the anticlinal wall, the lack of cell wall thickness differences between the anticlinal and periclinal walls, or boundary condition effects generated compressive forces[29]. Time and additional research will tell.

Conclusions and future perspectives. Our integrated experimental data and FE modelling analyses point to the central importance of the shared anticlinal wall[57] and the periclinal–anticlinal wall interface during mechanical signalling and polarized morphogenesis. The shared wall integrates stress patterns and growth status and determines the local rates and direction of growth. These new insights into pavement cell shape control provide a new way to integrate realistic cellular growth mechanisms into models that seek to explain how planar organs develop[58–61]. However, it is not known how stress- and microtubule-mediated growth patterns might scale to affect tissue-sector or organ morphology. The imaging locations here were primarily within the basal mid-blade of 1.5-DAG cotyledons, and the contributions of these cells and lobes to organ-scale shape change is not known. Organ-level leaf patterning is influenced by the patterned expression of combinations of proteins that somehow promote or limit growth[59,61]. Further analyses grounded in plausible FE growth models can reveal how morphogens, cell wall stress and cellular growth machineries interact to sculpt the macroscopic traits of leaves.

Methods

Plant material and growth conditions. *Arabidopsis thaliana* seedlings were grown at 22 °C on ½-strength Murashige and Skoog medium with 1% sucrose (w/v) and 0.8% (w/v) Bacto-agar under continuous illumination. For the chemical treatments, 1 µM oryzalin (Dow AgroSciences), 5 nM isoxaben (Sigma), 0.1% (v/v) DMSO (Sigma) and 0.2% (w/v) pectinase from *Aspergillus niger* (Sigma), the seeds were transferred and completely submerged in liquid media (which omits the Bacto-agar) after germination under continuous illumination. For low-light chemical treatment, the seedlings were grown on plain media until 1 DAG and then transferred to plates with the chemical compound dissolved onto the media, which were placed vertically at low light (5 µmol m^{-2} s^{-1}) at room temperature. *Arabidopsis* ecotype Columbia-0 was used as the wild type. The mutant lines were described previously: *any1* (ref. [31]), *qua2-1* (ref. [36]), *exo84b* (ref. [62]), *clasp1* (ref. [63]), *ktn1-2* (ref. [64]), *dis2-1* (ref. [41]), *zwi3* (ref. [65]) and *csi1-3* (ref. [39]). PDLP3::PDLP3–GFP[66] was crossed to the PIP2–mCherry line[67]. The double-tagged lines were described previously: PIP2–mCherry; TuB6–GFP double-tagged line[68]; and mCherry–Tua5; YFP–CesA6 (ref. [69]).

Imaging and analysis of cotyledon pavement cell shape: population-level studies. Whole seedlings were stained using 1 µM FM4-64 (Invitrogen) for 30 min at 4 °C. The cotyledons were dissected and mounted into a Vaseline-lined chamber slide and imaged using a Bio-Rad 2100 laser-scanning confocal microscope mounted on a Nikon Eclipse E800 stand. The samples were excited with a 488 nm laser, and the fluorescence signal was collected using a 490 nm long-pass dichroic and a 500 to 550 nm band-pass emission filter using a ×20 0.5 NA objective. Image fields were obtained from the apical third of the cotyledon. Representative complete pavement cells not part of the stomata cell linage were traced manually using the polygon tool in Fiji, and the traces were splined using the line-tool option. Pavement cell traces were analysed using LobeFinder[37], and the statistical analyses were done in RStudio (v.1.3.1093).

Imaging of CesA colocalization with microtubules. One-DAG seedlings were mounted on a Vaseline-lined chamber slice and imaged using a ×100 Plan-APO 1.46 NA oil-immersion objective, and images were acquired using a spinning disk CSU-10 confocal head (Yokogawa Electric) mounted on a Zeiss Observer. Z1 inverted microscope controlled using SlideBook software (Intelligent Imaging Innovation). YFP and mCherry were excited by 515 nm and 561 nm lasers, respectively. A single optical section of the outer periclinal wall was selected using the mCherry line. Imaging was conducted at 15-second intervals for 8 minutes, keeping the ROI in focus by using the mCherry line. Qualitative time-projected images were constructed after using the ImageJ bleach correction macro with the histogram matching method.

Centre of mass measurements and subsegmental growth rate analysis. For confocal microscopy and time-lapse imaging of lobe initiation, 1.5-DAG whole seedlings were mounted in our in-house long-term chamber system as previously described[26]. Confocal fluorescence microscopy was performed using a ×100 Plan-APO 1.46 NA oil-immersion objective, and images were acquired using a spinning disk CSU-10 confocal head (Yokogawa Electric) mounted on a Zeiss Oberver.Z1 inverted microscope controlled using SlideBook software (Intelligent Imaging Innovation). GFP and mCherry were excited by 488 nm and 561 nm laser lines, respectively. Approximately 10-min sequential image acquisition was performed for the microtubule and plasma-membrane time-lapses and half-hourly or hourly for the plasma-membrane and PDLP time-lapses using an Evolve 512 camera (Photometrics) through band-pass filters (482/35 and 617/73; Semrock). Segment length as a function of the segment's centre of mass was conducted by first saving the *xy* coordinates for both the initial and final time points in separate .csv files with *x* and *y* headings and then running the segmentLengthAFOCenterOfMass.py code. Segments with at least one PDLP were identified, and the three-way junctions were manually tagged using a three-by-three-pixel square 1.5 µm below the three-way junction for two image slices. Using the plasma membrane, cell boundaries spanning from slightly past the three-way junction were segmented manually using the segmented line tool with the spline function activated in Fiji and saved as an ROI. After all time points were collected, the ROI series were saved as a .zip file. The macro PDLP.ijm (which acted on both the plasma membrane and PDLP channels at each time point) straightened the segment and resliced the straightened segment, and then a max-projected image was produced. To reduce the tilt due to sample or mounting, one time point was aligned to the *x* axis using the three-way-junction marks, and the rest of the time points were aligned to it using resliceAlignment.ijm, which worked on lines drawn from three-way junction to three-way junction. PDLPs were tracked using the Particle Tracker 2D/3D tool from the MOSAIC imaging toolset[70]. Non-overlapping PDLPs at least 2 µm apart were used to calculate pairwise distance as a function of time. These values were used to obtain a linear fit equation, and its slope was used as the subsegmental growth rate; if the total displacement was less than the image resolution, then a growth rate of zero was awarded. To first verify that the PDLP movement reflected growth, the displacement of 14 PDLP pairs from 3 segments from 4 °C growth-inhibited seedlings was compared with the growth rate of 38 PDLP pairs from 12 segments from seedlings grown at 22 °C. To verify the accuracy of the PDLP subsegmental growth, the subsegment values were summed and evaluated to the displacement measured independently from the two endpoints defined by the three-way junctions. If the value was less than 3% error, the measurements were accepted. The subsegmental population-level analysis was conducted as follows: subsegments that occupied at least 60% of the lobe apex were classified as 'apex', subsegments that occupied at least 60% of the lobe flank were classified as 'flank' and everything else was classified as 'mixed'. All statistical analyses were conducted using RStudio (v.1.3.1093). Subsegmental growth rate plots were created in MATLAB (v.R2020a). Python (v.3.7.6) was run using Spyder IDE (v.4.0.1).

Imaging of delamination and furrows after pectinase treatment and TEM. The plasma membrane marker PIP2–mCherry was excited by the 561 nm laser line through bandpass filters as described above. For low-light chemical treatment, six to eight image fields at the basal region of the cotyledon were collected using the ×63 C-Apo 1.2 NA water immersion objective, and images were acquired using the Evolve 512 camera. For submerged chemical treatment, 1-DAG seedlings were placed in the chemical treatment for 24 hours; the then-2-DAG cotyledons were imaged completely using the ×20 Plan-APO 0.8 NA objective using a Prime 95B camera (Photometrics), and 3D montaging was done using the montage method in SlideBook. For TEM, leaf material was prepared as previously described[26].

FE model. Stress analysis in the pavement cell walls was studied using the commercial FE software Abaqus (2019). The structural model of the cells was based on the segmented cell wall boundary and surrounding anticlinal wall. All cells were divided by a middle lamellar layer of pectin. The model before the application of turgor pressure consisted of a flat periclinal wall bonded to the anticlinal walls. The thickness of the periclinal and anticlinal walls was 300 and 35 nm, respectively. All cells were surrounded with pectin to approximate the confinement of adjacent cells. The turgor pressure in each cell was 0.6 MPa. The material for all cells was assumed to be a neo-Hookean, hyperelastic isotropic material assigned uniformly across the model. The elastic modulus was assumed to be 600 MPa with a Poisson's ratio of 0.47. The whole material was assumed to be a standard linear solid with a primary relaxation time of 6.8 s and a ratio of infinite modulus to the total elastic modulus of 0.85 (ref. [71]). The middle lamellar pectin was assumed to have the same properties as the surrounding pectin with an elastic modulus of 100 MPa (ref. [72]). For all pairs of segmented cells, after 20 s of pressurization and sufficient relaxation, the stress field in the cell wall was used for analysis. For the segment of cells used to study the correlation of segmental growth rate and the associated σ_{max}, after the first step of 20 s of pressurization, the deformed structural model at the end of the first step was used as the initial structure in the second step and was pressurized for another 20 s, and then the stress field in the walls at the end of second step was used for analysis.

To demonstrate the influence of the concentrated microfibrils located in the cell connection boundary for the lobe formation, one pair of pavement cells was used for FE analysis. Considering the lobe formation during cell growth, the two cells were not confined using surrounding pectin; instead, pressures of 0.6 MPa were exerted uniformly across the outer side of the whole anticlinal walls. Turgor pressure in the cells was also set to 0.6 MPa. The inner periclinal walls were constrained in the vertical direction given the support by the underlying cells, and one local region (random position) of the anticlinal walls was constrained in the lateral directions to ensure the complete boundary conditions of the system. Three steps were set for the analysis. The periclinal wall in the zero step was flat before pressurization, and the inflated cell walls at the end of the previous step were used as the initial structural models of the next step. The loading time at each step was set to 30 s for sufficient relaxation. At the zero step, all the materials were assumed to be isotropic neo-Hookean hyperelastic material with a Young's modulus of 600 MPa and Poisson's ratio of 0.47, and they were assumed to be a standard linear solid with a primary relaxation time of 6.8 s and a ratio of infinite modulus to the total modulus of 0.85. In the first and second steps, for the initiating cell, a patch of anisotropic materials resembling a bundle of microfibrils was assigned for the local periclinal and associated anticlinal walls in the interaction region; this patch had a rectangular area of 2 µm × 4 µm in the periclinal wall. Local orthogonal material coordinates were defined for these materials in the region, with the *x* axis perpendicular to the boundary edge and the *y* axis parallel to the edge. The materials in this region were assumed to be transversely isotropic and to have a mechanical response prescribed by Hooke's law. The parameters of the constitutive equation include elastic moduli of E_{MF} = 2,400 MPa for microfibrils (where MF is parallel to microfibril orientation) and E_T = 240 MPa (where T is transverse to microfibril orientation), a shear modulus of $G_{MF\text{-}T}$ = 240 MPa and Poisson's ratios of $\nu_{MF\text{-}T}$ = 0.4 and $\nu_{T\text{-}T}$ = 0.47. The shear modulus, $G_{MF\text{-}T}$, represents the deformation resistance of the material to the external shear force which is applied parallel to one of the material surfaces (perpendicular to the MF orientation) and pointing in the T direction. The modulus E_{MF} was set in the *x* axis, and E_T was defined along the *y* and *z* axes. A reference FE example was made to compare with the effect of the presence of the anisotropic patch. In the reference example, all the cell walls across the three steps were assumed to be isotropic neo-Hookean hyperelastic material. At the end of the final step, the connection boundary in both the reference example and the model using the anisotropic patch was used for comparison.

Anticlinal wall tilt analysis. Segment shapes were traced as explained above. Lobes and their locations were identified by using the find_peaks and peaks_prominences modules in Python restricted to features greater than 286 nm as previously described[13]. To get the local tilt at the apex as a function of lobe formation, the relative position of the lobe in a normalized length was used to get its relative position prior to the lobe detection. A reslice of the anticlinal wall at the apex was traced using the segmented line tool in Fiji for a time point before lobe detection, a time point at detection and at least one time point after detection. The traces were analysed by first rotating them to the *y* axis and then measuring their width, giving a score of zero to widths smaller than the imaging resolution. The OrientationJ Dominant Direction plug-in was used to obtain the tilt along the segment[73].

Selection of time intervals for microtubule imaging. Single images and image stack time-lapses were first run through the background reduction as previously described[13]. The image stacks were max-projected. Time-lapses were registered using rigid registration in StackReg using the MT channel. ROIs were selected and cropped. Each time point was saved as a text image. The Python code normalizedTextImageDataAndCorrelation.py was run, which first normalizes each image from 0 to 1. Spearman correlations were then conducted between the initial time point and all time points, in a moving window comparing a time point with the next time point and finally between each time point and a randomly selected time point. The mean Spearman correlation value for all columns was obtained for each comparison type listed above as a function of time. The values were then plotted. The statistical analysis and plots were done in Python (v.3.7.6) using Spyder IDE (v.4.0.1).

Microtubule persistence at the anticlinal and outer periclinal walls for neighbouring cells. Using the segment traces generated as described above, the .zip file for a segment's time-series was run through the imageTextOfMTWalls.ijm macro, which allows the extraction of the microtubule signal from the anticlinal and outer periclinal walls. For each time point, the segment was straightened and resliced, and a SUM projected image was created of the plasma membrane, which allows the user to create a bounding box that defines the extent of the anticlinal wall on the image stack. This information was propagated to the microtubule channel. A text image of the outer periclinal wall for each neighbouring cell after a MAX intensity projection was produced. A text image of the anticlinal wall after SUM projection of six resliced images was also produced. To create the persistence peaks of microtubules for all three cell wall views, the Python code createAnticlinalAndOuterPericlinalPersistenceMaps.py was run. This requires information about which cell is the initiating cell, at what time point the lobe is detected, the location of the lobe at detection and the width of the lobe apex at detection. For each time point, using the three matrices produced by imageTextOfMTWalls.ijm, the columns were summed to obtain a line plot for each of the cell wall views. The values for the anticlinal wall were normalized from zero to one using the equation:

$$\text{normValue} = \frac{\text{Value}_i - \min(\text{array})}{\max(\text{array}) - \min(\text{array})}$$

For the periclinal wall, the values were normalized from zero to one using the maxima and minima of both datasets combined. Stack plots were created using the normalized values for the time points before lobe initiation, after lobe initiation and for the whole time-lapse. Microtubule enrichment was calculated by obtaining the area under the curve, using the trapezoid method, of the accumulated microtubule plots at the lobe apex. The enrichment was calculated using the following equation:

$$\text{Enrichment} = -1 + \frac{\text{Area}_{\text{Cell1}}}{\text{Area}_{\text{Cell2}}} \times 100$$

This was also done at each time point individually to obtain the enrichment at each time point.

Microtubule orientation and coherency analysis. Segments of interest were aligned to the first time point by drawing a line across the three-way junctions and saving them as ROIs. The regIndSegWith3WJLines.ijm macro was then run, which requires the user to select the location for the folder containing the max-projected images, the ROI .zip file location from three-way-junction lines and an output folder. The location of a new lobe was then identified as explained above, and two 2 µm × 2 µm ROIs were placed across the anticlinal wall at the location where a new lobe will form. The OrientationJ Dominant Direction plug-in was used to obtain the orientation and coherency of microtubules. The plots were created in Python (v.3.7.6) using Spyder IDE (v.4.0.1).

Manual transfacial microtubule scoring. Text image outputs from imageTextOfMTWalls.ijm were imported into Fiji and converted to RGB colour. To observe which bundles were transfacial, it was necessary to combine the anticlinal and outer periclinal wall images using the combine tool in Fiji. The images were combined vertically, with the anticlinal wall positioned directly below the outer periclinal wall that corresponded to the same time point. This was done for both cells that shared the anticlinal wall. Transfacial microtubule bundles were then scored by marking them in the middle of the bundle. Only clear, distinct transfacial microtubule bundles were scored, which we defined as microtubules that directly connected from the anticlinal wall into the outer periclinal wall. These bundles appear as a continuous, vertical line of high-intensity pixels in the combined image. The pixel locations for all marked transfacial microtubule bundles, along with the pixel width of the entire image, were recorded to generate normalized segment length histograms. A density curve was obtained using these values. To match the *y* value range to the histogram, the density values were multiplied by the proportional difference between the maximal value of the density plot and the maximal value of the histogram graph. The plots were created in RStudio (v.1.3.1093).

Microtubule organization within furrows and furrow position on straight segments. Nascent furrows, obtained using the methods described above, were traced to and from regions where the anticlinal wall separated. For each furrow, the microtubule intensity was measured at the anticlinal wall and then normalized from 0 to 1. The length of each furrow was normalized from 0 to 1. A stack plot from 36 nascent furrows from 5 cotyledons was constructed of the normalized signal to obtain a population-level plot of microtubule preference within a furrow. The location of a furrow within a segment was obtained from the normalized peak location of a subset of nascent furrows from straight segments (23 segments from 5 cotyledons), and a histogram was created using RStudio. The plots were created in Python (v.3.7.6) using Spyder IDE (v.4.0.1).

Statistics and reproducibility. No statistical method was used to predetermine sample size. No data were excluded from the analyses. The experiments were not randomized. We were not blinded to allocation during the experiments and outcome assessment. Two-sided Wilcoxon rank-sum tests were used to test the significance of normalized growth rate between segment subregions, cell metrics between wild-type and mutant populations, and cell metrics between control conditions and pharmacological treatments. The PDLP strain measurements come from five independent imaging time-lapses with a total of 41 segments. The cell wall stress simulations of lobing cells were obtained from three independent models. The transfacial microtubule analyses were conducted on six independent imaging time-lapses with a total of 12 segments. To demonstrate the correlation of PDLP strain with the cell wall stress pattern, two independent FE simulations/time-lapses were conducted for five pairs of cells. The analyses of stress patterns based on remaining cell wall percentage come from three independent FE simulations for three cell segments. For the comparison of stress pattern and the associated microtubule accumulation, cell wall stress analyses were obtained from five independent FE simulations. For the segments of cells with a furrow, two independent FE simulations were conducted for two cell segments.

Reporting Summary. Further information on research design is available in the Nature Research Reporting Summary linked to this article.

Data availability

The Fiji macros, Python scripts and PDLP growth rate code in R used for all image analyses are available at https://github.com/yamsissamy/naturePlant_lobeInitiation. Abaqus input files for the FE models shown in the figures are available at http://tulips.unl.edu.

Received: 26 August 2020; Accepted: 28 April 2021;
Published online: 10 June 2021

References

1. Chitwood, D. H. & Sinha, N. R. Evolutionary and environmental forces sculpting leaf development. *Curr. Biol.* **26**, R297–R306 (2016).
2. Swarup, R. et al. Localization of the auxin permease AUX1 suggests two functionally distinct hormone transport pathways operate in the *Arabidopsis* root apex. *Genes Dev.* **15**, 2648–2653 (2001).
3. Savaldi-Goldstein, S., Peto, C. & Chory, J. The epidermis both drives and restricts plant shoot growth. *Nature* **446**, 199–202 (2007).
4. Vaseva, I. I. et al. The plant hormone ethylene restricts *Arabidopsis* growth via the epidermis. *Proc. Natl Acad. Sci. USA* **115**, E4130–E4139 (2018).
5. Andriankaja, M. et al. Exit from proliferation during leaf development in *Arabidopsis thaliana*: a not-so-gradual process. *Dev. Cell* **22**, 64–78 (2012).
6. Das Gupta, M. & Nath, U. Divergence in patterns of leaf growth polarity is associated with the expression divergence of miR396. *Plant Cell* **27**, 2785–2799 (2015).
7. Vofely, R. V., Gallagher, J., Pisano, G. D., Bartlett, M. & Braybrook, S. A. Of puzzles and pavements: a quantitative exploration of leaf epidermal cell shape. *New Phytol.* **221**, 540–552 (2019).
8. Haberlandt, G. *Physiological Plant Anatomy* 4th edn (MacMillan, 1914).
9. Panteris, E. & Galatis, B. The morphogenesis of lobed plant cells in the mesophyll and epidermis: organization and distinct roles of cortical microtubules and actin filaments. *New Phytol.* **167**, 721–732 (2005).

10. Fu, Y., Gu, Y., Zheng, Z., Wasteneys, G. & Yang, Z. *Arabidopsis* interdigitating cell growth requires two antagonistic pathways with opposing action on cell morphogenesis. *Cell* **120**, 687–700 (2005).
11. Szymanski, D. B. The kinematics and mechanics of leaf expansion: new pieces to the *Arabidopsis* puzzle. *Curr. Opin. Plant Biol.* **22C**, 141–148 (2014).
12. Gao, Y. et al. Auxin binding protein 1 (ABP1) is not required for either auxin signaling or *Arabidopsis* development. *Proc. Natl Acad. Sci. USA* **112**, 2275–2280 (2015).
13. Belteton, S. A., Sawchuk, M. G., Donohoe, B. S., Scarpella, E. & Szymanski, D. B. Reassessing the roles of PIN proteins and anticlinal microtubules during pavement cell morphogenesis. *Plant Physiol* **176**, 432–449 (2018).
14. Xu, T. et al. Cell surface- and Rho GTPase-based auxin signaling controls cellular interdigitation in *Arabidopsis*. *Cell* **143**, 99–110 (2010).
15. Armour, W. J., Barton, D. A., Law, A. M. & Overall, R. L. Differential growth in periclinal and anticlinal walls during lobe formation in *Arabidopsis* cotyledon pavement cells. *Plant Cell* **27**, 2484–2500 (2015).
16. Sapala, A. et al. Why plants make puzzle cells, and how their shape emerges. *eLife* https://doi.org/10.7554/eLife.32794 (2018).
17. Altartouri, B. et al. Pectin chemistry and cellulose crystallinity govern pavement cell morphogenesis in a multi-step mechanism. *Plant Physiol.* **181**, 127–141 (2019).
18. Haas, K. T., Wightman, R., Meyerowitz, E. M. & Peaucelle, A. Pectin homogalacturonan nanofilament expansion drives morphogenesis in plant epidermal cells. *Science* **367**, 1003–1007 (2020).
19. Elsner, J., Lipowczan, M. & Kwiatkowska, D. Differential growth of pavement cells of *Arabidopsis thaliana* leaf epidermis as revealed by microbead labeling. *Am. J. Bot.* **105**, 257–265 (2018).
20. Sampathkumar, A. et al. Subcellular and supracellular mechanical stress prescribes cytoskeleton behavior in *Arabidopsis* cotyledon pavement cells. *eLife* **3**, e01967 (2014).
21. Zhang, C., Halsey, L. E. & Szymanski, D. B. The development and geometry of shape change in *Arabidopsis thaliana* cotyledon pavement cells. *BMC Plant Biol.* **11**, 27 (2011).
22. Elsner, J., Michalski, M. & Kwiatkowska, D. Spatiotemporal variation of leaf epidermal cell growth: a quantitative analysis of *Arabidopsis thaliana* wild-type and triple cyclinD3 mutant plants. *Ann. Bot.* **109**, 897–910 (2012).
23. Paredez, A. R., Somerville, C. R. & Ehrhardt, D. W. Visualization of cellulose synthase demonstrates functional association with microtubules. *Science* **312**, 1491–1495 (2006).
24. Baskin, T. I. Anisotropic expansion of the plant cell wall. *Annu. Rev. Cell Dev. Biol.* **21**, 203–222 (2005).
25. Green, P. B. The spiral growth pattern of the cell wall in *Nitella axillaris*. *Am. J. Bot.* **41**, 403–409 (1954).
26. Yanagisawa, M. et al. Patterning mechanisms of cytoskeletal and cell wall systems during leaf trichome morphogenesis. *Nat. Plants* **1**, 15014 (2015).
27. Wong, J. H. et al. Basic proline-rich protein-mediated microtubules are essential for lobe growth and flattened cell geometry. *Plant Physiol.* **181**, 1535–1551 (2019).
28. Majda, M. et al. Mechanochemical polarization of contiguous cell walls shapes plant pavement cells. *Dev. Cell* **43**, 290–304 (2017).
29. Bidhendi, A. J., Altartouri, B., Gosselin, F. P. & Geitmann, A. Mechanical stress initiates and sustains the morphogenesis of wavy leaf epidermal cells. *Cell Rep.* **28**, 1237–1250 (2019).
30. Fayant, P. et al. Finite element model of polar growth in pollen tubes. *Plant Cell* **22**, 2579–2593 (2010).
31. Fujita, M. et al. The *anisotropy1* D604N mutation in the *Arabidopsis* cellulose synthase1 catalytic domain reduces cell wall crystallinity and the velocity of cellulose synthase complexes. *Plant Physiol.* **162**, 74–85 (2013).
32. Uyttewaal, M. et al. Mechanical stress acts via katanin to amplify differences in growth rate between adjacent cells in *Arabidopsis*. *Cell* **149**, 439–451 (2012).
33. Ambrose, J. C., Shoji, T., Kotzer, A. M., Pighin, J. A. & Wasteneys, G. O. The *Arabidopsis* CLASP gene encodes a microtubule-associated protein involved in cell expansion and division. *Plant Cell* **19**, 2763–2775 (2007).
34. Kotzer, A. M. & Wasteneys, G. O. Mechanisms behind the puzzle: microtubule–microfilament cross-talk in pavement cell formation. *Can. J. Bot.* **84**, 594–603 (2006).
35. Whittington, A. T. et al. MOR1 is essential for organizing cortical microtubules in plants. *Nature* **411**, 610–613 (2001).
36. Mouille, G. et al. Homogalacturonan synthesis in *Arabidopsis thaliana* requires a Golgi-localized protein with a putative methyltransferase domain. *Plant J.* **50**, 605–614 (2007).
37. Wu, T.-C., Belteton, S. A., Pack, J., Szymanski, D. B. & Umulis, D. M. LobeFinder: a convex-hull based method for quantitative boundary analysis of lobed plant cells. *Plant Physiol.* **171**, 2331–2342 (2016).
38. Paredez, A. R., Persson, S., Ehrhardt, D. W. & Somerville, C. Genetic evidence that cellulose synthase activity influences microtubule cortical array organization. *Plant Physiol.* **147**, 1723–1734 (2008).
39. Li, S., Lei, L., Somerville, C. R. & Gu, Y. Cellulose synthase interactive protein 1 (CSI1) links microtubules and cellulose synthase complexes. *Proc. Natl Acad. Sci. USA* **109**, 185–190 (2012).
40. Staff, L. et al. The hidden geometries of the *Arabidopsis thaliana* epidermis. *PLoS ONE* **7**, e43546 (2012).
41. El-Assal, S. E., Le, J., Basu, D., Mallery, E. L. & Szymanski, D. B. *DISTORTED2* encodes an ARPC2 subunit of the putative *Arabidopsis* ARP2/3 complex. *Plant J.* **38**, 526–538 (2004).
42. Harris, W. M. Ultrastructural observations on the mesophyll cells of pine leaves. *Can. J. Bot.* **49**, 1107–1109 (1971).
43. Verger, S., Long, Y., Boudaoud, A. & Hamant, O. A tension–adhesion feedback loop in plant epidermis. *eLife* https://doi.org/10.7554/eLife.34460 (2018)
44. Apostolakos, P., Galatis, B. & Panteris, E. Microtubules in cell morphogenesis and intercellular space formation in *Zea mays* leaf mesophyll and *Pilea cadierei* epithem. *J. Plant Physiol.* **137**, 591–601 (1991).
45. Panteris, E., Apostolakos, P. & Galatis, B. Microtubule organization and cell morphogenesis in two semi-lobed cell types of *Adiantum capillus-veneris* L. leaflets. *New Phytol.* **125**, 509–520 (1993).
46. Panteris, E., Apostolakos, P. & Galatis, B. Sinuous ordinary epidermal cells: behind several patterns of waviness, a common morphogenetic mechanism. *New Phytol.* **127**, 771–780 (1994).
47. Fu, Y., Li, H. & Yang, Z. The ROP2 GTPase controls the formation of cortical fine F-actin and the early phase of directional cell expansion during *Arabidopsis* organogenesis. *Plant Cell* **14**, 777–794 (2002).
48. Fu, Y., Gu, Y., Zheng, Z., Wasteneys, G. & Yang, Z. *Arabidopsis* interdigitating cell growth requires two antagonistic pathways with opposing action on cell morphogenesis. *Cell* **120**, 687–700 (2005).
49. Kutschera, U., Bergfeld, R. & Schopfer, P. Cooperation of epidermis and inner tissues in auxin-mediated growth of maize coeloptiles. *Planta* **170**, 168–180 (1987).
50. Chan, J. & Coen, E. Interaction between autonomous and microtubule guidance systems controls cellulose synthase trajectories. *Curr. Biol.* **30**, 941–947 (2020).
51. Elliott, A. & Shaw, S. L. Microtubule array patterns have a common underlying architecture in hypocotyl cells. *Plant Physiol.* **176**, 307–325 (2018).
52. Xu, T. et al. Cell surface ABP1–TMK auxin-sensing complex activates ROP GTPase signaling. *Science* **343**, 1025–1028 (2014).
53. Zhao, F. et al. Microtubule-mediated wall anisotropy contributes to leaf blade flattening. *Curr. Biol.* **30**, 3972–3985 (2020).
54. Ren, T., Weraduwage, S. M. & Sharkey, T. D. Prospects for enhancing leaf photosynthetic capacity by manipulating mesophyll cell morphology. *J. Exp. Bot.* **70**, 1153–1165 (2019).
55. He, W., Adachi, S., Sage, R. F., Ookawa, T. & Hirasawa, T. Leaf photosynthetic rate and mesophyll cell anatomy changes during ontogenesis in backcrossed indica × japonica rice inbred lines. *Photosynth. Res.* **134**, 27–38 (2017).
56. Higaki, T. et al. A theoretical model of jigsaw-puzzle pattern formation by plant leaf epidermal cells. *PLoS Comput. Biol.* **12**, e1004833 (2016).
57. Jarvis, M. C., Briggs, S. P. H. & Knox, J. P. Intercellular adhesion and cell separation in plants. *Plant Cell Environ.* **26**, 977–989 (2003).
58. Rolland-Lagan, A.-G., Bangham, J. A. & Coen, E. Growth dynamics underlying petal shape and asymmetry. *Nature* **422**, 161–163 (2003).
59. Kuchen, E. E. et al. Generation of leaf shape through early patterns of growth and tissue polarity. *Science* **335**, 1092–1096 (2012).
60. Hervieux, N. et al. A mechanical feedback restricts sepal growth and shape in *Arabidopsis*. *Curr. Biol.* https://doi.org/10.1016/j.cub.2016.03.004 (2016).
61. Kierzkowski, D. et al. A growth-based framework for leaf shape development and diversity. *Cell* **177**, 1405–1418 (2019).
62. Fendrych, M. et al. The *Arabidopsis* exocyst complex is involved in cytokinesis and cell plate maturation. *Plant Cell* **22**, 3053–3065 (2010).
63. Ambrose, C., Allard, J. F., Cytrynbaum, E. N. & Wasteneys, G. O. A CLASP-modulated cell edge barrier mechanism drives cell-wide cortical microtubule organization in *Arabidopsis*. *Nat. Commun.* **2**, 430 (2011).
64. Nakamura, M., Ehrhardt, D. W. & Hashimoto, T. Microtubule and katanin-dependent dynamics of microtubule nucleation complexes in the acentrosomal *Arabidopsis* cortical array. *Nat. Cell Biol.* **12**, 1064–1070 (2010).
65. Oppenheimer, D. G. et al. Essential role of a kinesin-like protein in *Arabidopsis* trichome morphogenesis. *Proc. Natl Acad. Sci. USA* **94**, 6261–6266 (1997).
66. Thomas, C. L., Bayer, E. M., Ritzenthaler, C., Fernandez-Calvino, L. & Maule, A. J. Specific targeting of a plasmodesmal protein affecting cell-to-cell communication. *PLoS Biol.* **6**, e7 (2008).
67. Nelson, B. K., Cai, X. & Nebenfuhr, A. A multicolored set of in vivo organelle markers for co-localization studies in *Arabidopsis* and other plants. *Plant J.* **51**, 1126–1136 (2007).
68. Belteton, S. A., Sawchuk, M. G., Donohoe, B. S., Scarpella, E. & Szymanski, D. B. Reassessing the roles of PIN proteins and anticlinal microtubules during pavement cell morphogenesis. *Plant Physiol.* **176**, 432–449 (2018).

69. Gutierrez, R., Lindeboom, J. J., Paredez, A. R., Emons, A. M. & Ehrhardt, D. W. *Arabidopsis* cortical microtubules position cellulose synthase delivery to the plasma membrane and interact with cellulose synthase trafficking compartments. *Nat. Cell Biol.* **11**, 797–806 (2009).
70. Sbalzarini, I. F. & Koumoutsakos, P. Feature point tracking and trajectory analysis for video imaging in cell biology. *J. Struct. Biol.* **151**, 182–195 (2005).
71. Forouzesh, E., Goel, A., Mackenzie, S. A. & Turner, J. A. In vivo extraction of *Arabidopsis* cell turgor pressure using nanoindentation in conjunction with finite element modeling. *Plant J.* **73**, 509–520 (2013).
72. Zsivanovits, G., MacDougall, A. J., Smith, A. C. & Ring, S. G. Material properties of concentrated pectin networks. *Carbohydr. Res.* **339**, 1317–1322 (2004).
73. Puspoki, Z., Storath, M., Sage, D. & Unser, M. Transforms and operators for directional bioimage analysis: a survey. *Adv. Anat. Embryol. Cell Biol.* **219**, 69–93 (2016).

Acknowledgements

We thank D. Jackson (Cold Spring Harbor Laboratory) for his generous gift of the PDLP3–GFP transgenic line and Y. Gu (Pennsylvania State University) for her generous gift of the *csi1-3* mutant and *csi1-3*; YFP–CesA6; RFP–TUA5 transgenic line. This material is based on work supported by the National Science Foundation under grant no. 1715544 to D.B.S. and J.A.T.

Author contributions

D.B.S. and S.A.B. conceptualized the project. S.A.B. and W.L. developed the methodology. S.A.B., W.L., M.Y., M.I.Q., M.K.S., M.W.M. and F.A.H. conducted the investigation. S.A.B. and D.B.S. wrote the original draft. S.A.B., W.L., M.Y., M.I.Q., M.K.S., M.W.M., F.A.H., J.A.T. and D.B.S. reviewed and edited the draft. D.B.S. administered the project. D.B.S. and J.A.T. acquired the funding.

Competing interests

The authors declare no competing interests.

Additional information

Extended data is available for this paper at https://doi.org/10.1038/s41477-021-00931-z.

Supplementary information The online version contains supplementary material available at https://doi.org/10.1038/s41477-021-00931-z.

Correspondence and requests for materials should be addressed to D.B.S.

Peer review information *Nature Plants* thanks Olivier Hamant and the other, anonymous, reviewer(s) for their contribution to the peer review of this work.

Reprints and permissions information is available at www.nature.com/reprints.

Publisher's note Springer Nature remains neutral with regard to jurisdictional claims in published maps and institutional affiliations.

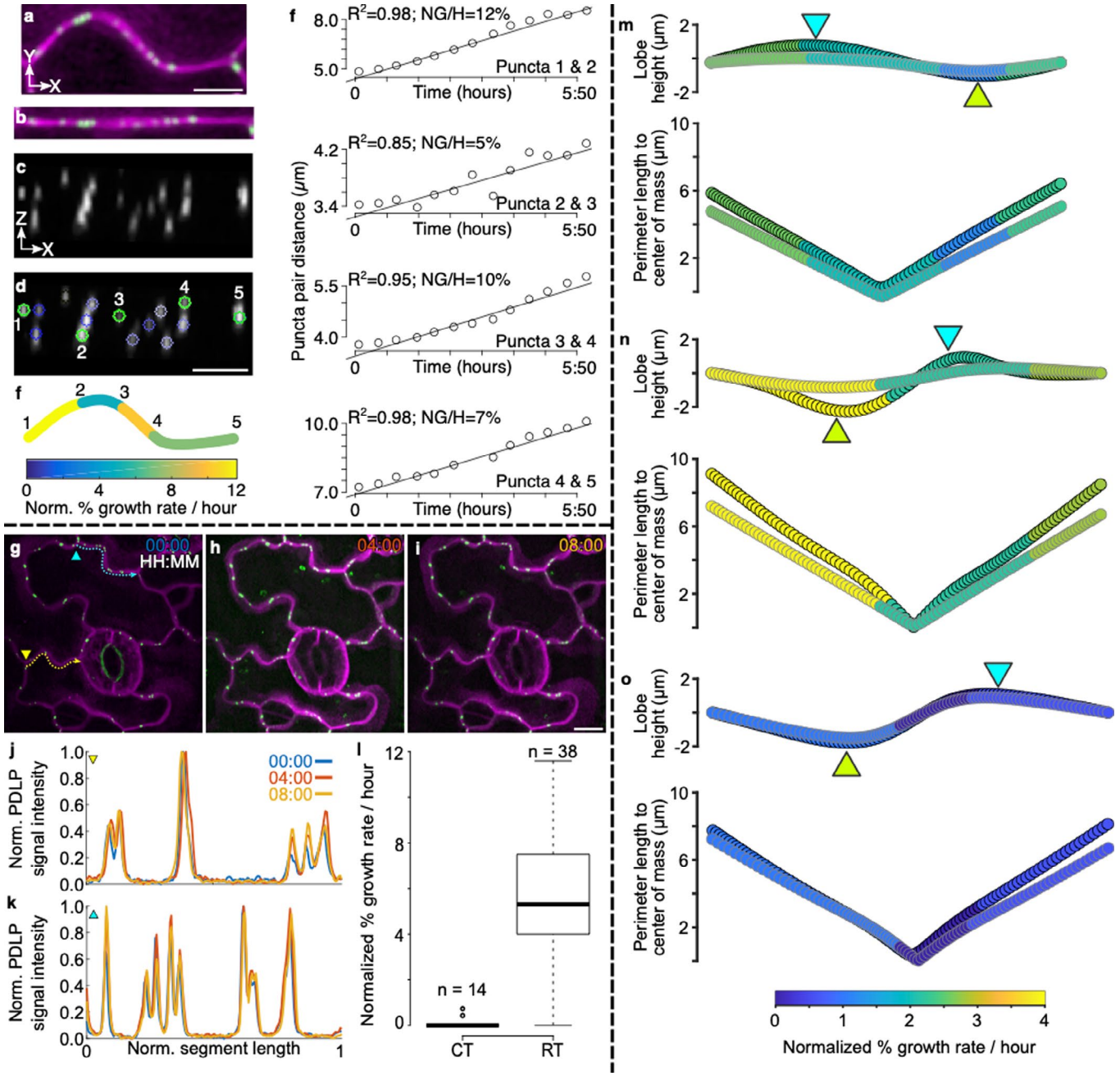

Extended Data Fig. 1 | Methodology for PDLP growth analysis, their reliability as fiducial marks, and their usage in lobing segments. Growth dependent separation of PDLP puncta pairs along an example segment. **a**, Using the plasma-membrane marker segments were traced at the anticlinal/outer-periclinal junction. **b**-**c**, Segment straightening followed by re-slicing produces a face-view of the anticlinal wall. **d**, Non-overlapping PDLPs including manually labeled 3-way-junctions were tracked over time. **e**, PDLP-pair distance is used to obtain sub-segmental growth rates from linear fit models over the time course. **f**, Sub-segmental elemental growth rates mapped onto the initial segment shape. PDLPs are stable features in the anticlinal wall and their displacement reflects localized diffuse growth. **g**-**i**, Cold-treated PDLP3:GFP; PIP2:mCherry seedlings were imaged at 4-hour intervals. **j**-**k**, Normalized signal intensity plots and overlapping peaks from PDLP3 particles of the two segments (**g**-**i**) at all 3 time-points. **l**, Boxplots of measured sub-segmental growth rates of cold-treated (CT) and room temperature (RT) grown seedlings. Center lines show the medians; box limits indicate the 25th and 75th percentiles as determined by R software; whiskers extend 1.5 times the interquartile range from the 25th and 75th percentiles, outliers are represented by dots. n = 14, 38 sub-segments from 3 and 9 independent segments respectively. Sub-segmental growth rates from lobing segments. **m**-**o**, Plots of normalized segment length at lobe detection (gray outline) and final (black outline) time-points color coded for normalized percent growth rate per hour. Cyan and green arrowheads mark the location of newly and established lobes respectively (Top panel). Perimeter to center of mass plots highlight warping regions between lobe detection and final timepoint. Scale bar = 5 μm (a-d), 10 μm (g-i).

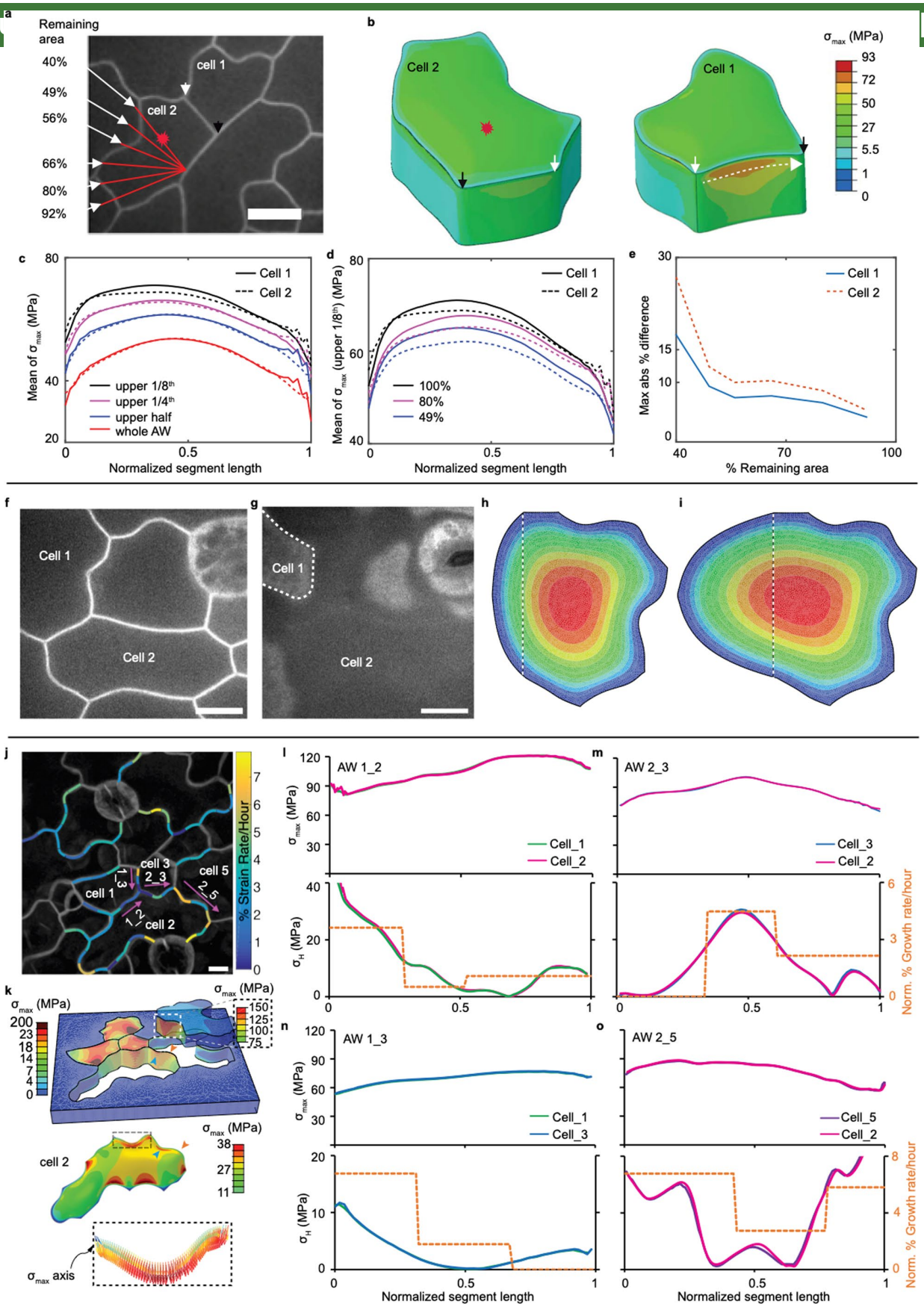

Extended Data Fig. 2 | See next page for caption.

Extended Data Fig. 2 | FE model optimization and correlation of maximum principal stress orientation with subsegment growth rate. a, Microscopic image of the cells which were used to study the effect of the partial geometry of cells for the stress response under turgor pressure. The star shows the location of the maximum deflection of the periclinal wall for Cell 2. **b**, 3D finite element (FE) model of the two complete cells and the distribution of maximum principal stress (Max PS) on both anticlinal walls (AW). **c**, Distribution of the mean of the Max PS from the upper 1/8th of the AW for both cells for three example results of partial cells in terms of the area used in the analysis. **d**, Maximum of the absolute value of the percentage difference between mean Max PS distributions in the upper 1/8th of the AW in each simulation relative to using the complete geometry of cells. It indicates that the FE analysis can use a partial cell. If the area includes the maximum deflection the distribution of the Max PS does not change substantially and the magnitude is reduced by < 10%. **e**, Comparison of the average of Max PS from the different upper areas of materials in the AW. It turns out that the mean of Max PS of the different upper areas in the walls has the same distribution pattern but varies in magnitude. **f**, Optical image of the cells were used to study the correlation of the Max PS and the growth rate of the cell-cell interfaces. **g**, Cell 2 from the measurement is defined partially, but the maximum deflection area can be seen in the image. **h**,**i**, Comparison of maximum deflection of periclinal wall for Cell 2 in (**f**–**g**) from the simulations using different remaining areas of the cell. The results of (**i**) is very consistent with the optical measurement in (**g**). **j**–**l**, Like the study described in (**f**), four other segments of cells were used for the comparison, and the results show that the horizontal component of Max PS along the segment length has a strong correlation with the growth rate of the associated wall. The scale bar for all = 10 μm.

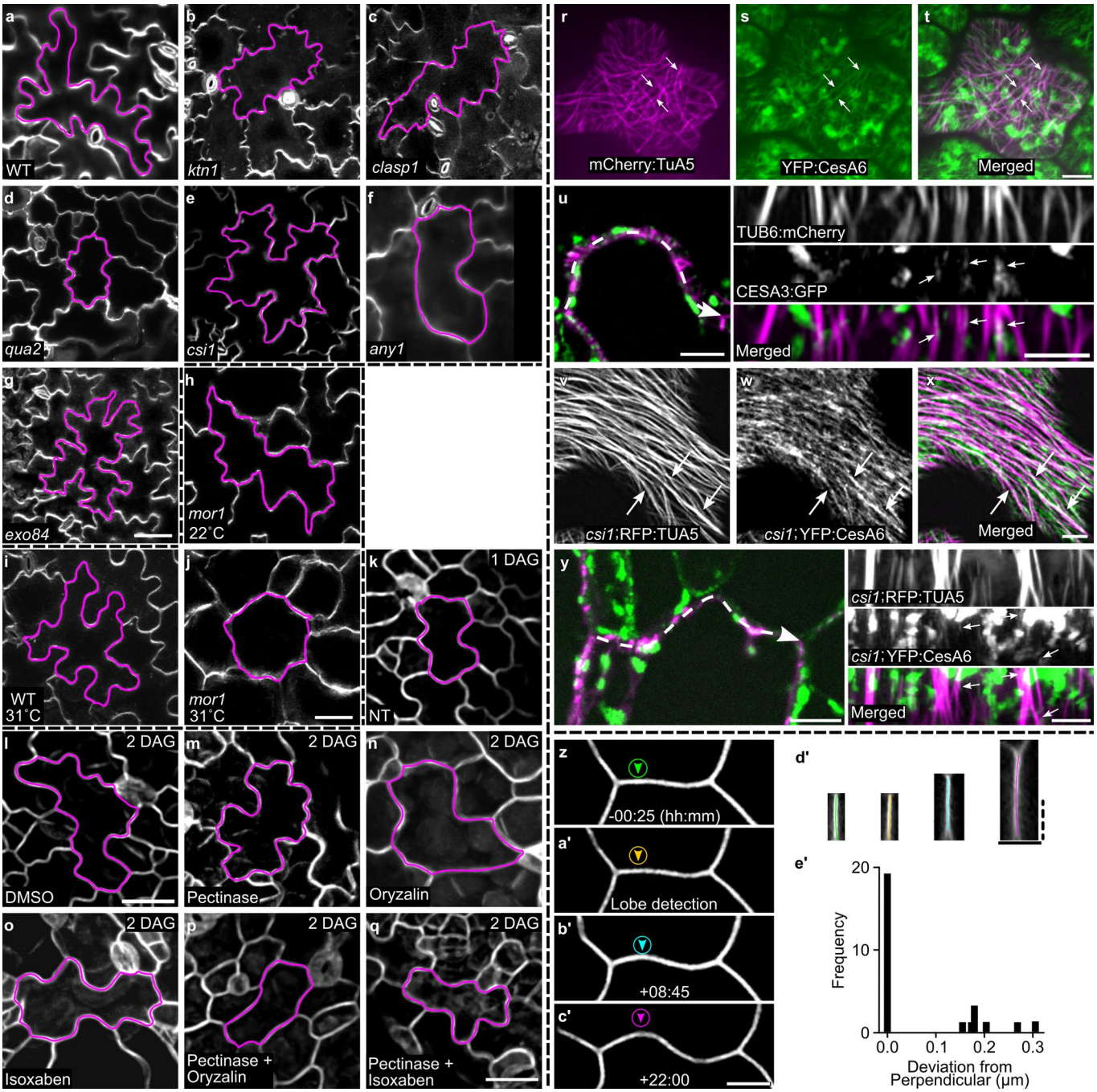

Extended Data Fig. 3 | The microtubule and cellulose systems are required for lobe formation. Mature pavement cell shapes, magenta outline, were analyzed using LobeFinder. Mutants affecting the microtubule- (**b**, **c**, **i-k**), cellulose- (**d**, **e**), and pectinase- (**f**), and secretion (**g**) were compared to wild-type (**a**, i). The temperature-sensitive mutant *mor1-1* was tested at permissive (**h**) and restrictive temperatures (**j**) and compared to its wild-type counterpart (**i**). Effects of 0.2% pectinase (**m**), 1 µM oryzalin (**n**), and 5 nM Isoxaben (**o**) on cell shape from 1 to 2 DAG compared to a buffer treated control (**l**). A combination of 0.2% Pectinase with a reduced concentration of Oryzalin [1 µM] (**p**) and the combination of 0.2% Pectinase and 5 nM Isoxaben (**q**) both completely halted the production on new lobes (Supplementary Table 1 – for results). Cellulose synthase complex marked with YFP:CesA6 strongly colocalizes with cortical microtubules in early stage pavement cells. **s**, 8-min projection of 15-sec intervals, single plane time course shows how CesA tracks resemble and co-localize (**t** – white arrows) with cortical microtubules, mCherry:TuA5 (**r**). Evidence of colocalization between cellulose synthase complex marked with CesA3:GFP and cortical microtubules at the anticlinal wall. **u**, Top-down view of segment resliced. Dotted line shows shape and direction of segmentation. White arrows on resliced images are CesA complexes that localized to anticlinal microtubules. The colocalization of cellulose and microtubules was not affected in 8-minute projection of 15-sec intervals, single plane time-lapses, in the *csi1* mutant background where CesA tracks (YFP:CesA6 - **w**) resemble and co-localized (**x** – white arrows) with cortical microtubules, RFP:TUA5 (**v**). Resliced views of the anticlinal wall also show evidence of cellulose and microtubule co-localization in the *csi1* mutant. CesA colocalization with anticlinal microtubules is evident in the *csi1* mutant background. **y**, Top-down view of segment resliced with dotted line showing the shape and direction of segmentation. White arrows on resliced images on the right are CesA complexes that localize to anticlinal microtubules. The anticlinal wall at the apex remains straight during lobe formation. **z**, Snapshots of a lobing segment before, (**a'**) during, (**b'**-**c'**) and after lobe formation. **d'**, Cross-sectional views of the anticlinal wall at the lobe apex from locations specified in (**z**-**c'**). **e'**, Histogram of anticlinal wall tilt showing how the vast majority of measure wall regions were completely perpendicular to the leaf surface. Scale bars = 50 µm (**a**-**q**), 25 µm (**k**-**q**), 5 µm (**r**-**d'**).

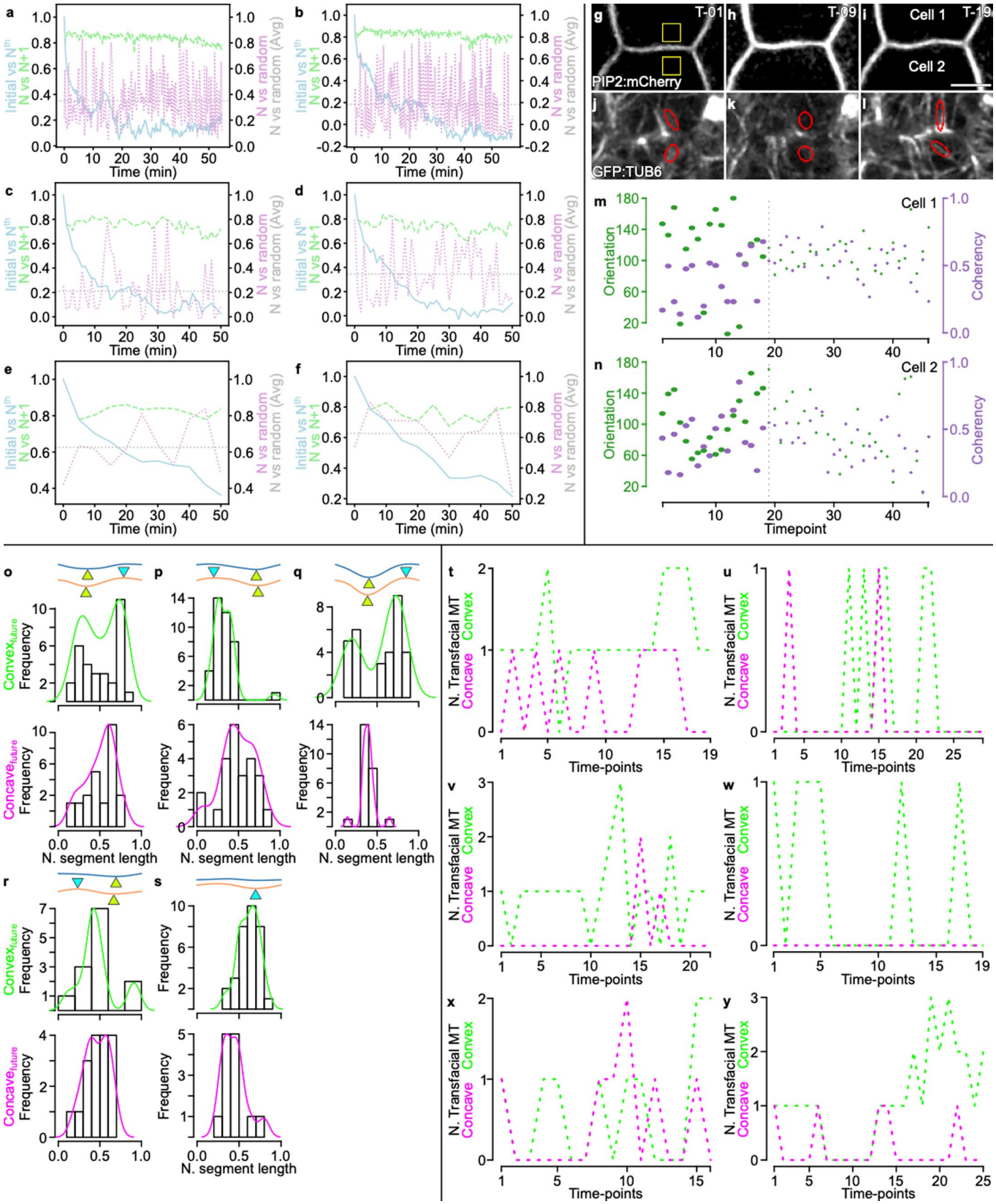

Extended Data Fig. 4 | See next page for caption.

Extended Data Fig. 4 | Transfacial microtubule localization and frequency analyses as a function of lobe initiation. Analysis of microtubule turnover in time series data. Pairwise correlation results between the initial time-point and each subsequent time-point (blue line), a sliding window of paired consecutive frames over the time course (green dashed line), and each time-point to a randomly selected time-point (magenta dotted line). The random correlation results average (gray dotted line) is the background level for microtubule correlations. **a**-**b**, 15-sec interval time-lapses. **c**-**d**, 1-min interval time-lapses. **e**-**f**, 5-minute interval time-lapses. Each sampling regime had a similar pattern of correlation decay from the first time-point to background levels after ~10 min. Microtubule orientation in ROIs in opposing cells that undergo lobe initiation does not show detectable differences in alignment and coherence. **g**-**i**, Snapshots of plasma-membrane (PIP2:mCherry) of a lobing segment, yellow boxes are ROIs used to monitor microtubule behaviors in opposing cells lobe centered at the future lobe region. **j**-**l**, Snapshots of the microtubules (GFP:TUB6). Microtubules orientation and coherency results using red ovals whose tilt reflects the orientation and their aspect ratios reflect the coherency of the microtubules at the time point shown. **m**-**n**, Scatterplot of microtubules orientation (green) and microtubule coherency (purple) in cell 1 (**g** -top) and cell 2 (**g** - bottom) as a function of time before (< time-point 19) and after (≥ time-point 19) lobe detection. Distribution of manually identified transfacial microtubules in lobing segments. **o**-**s**, Top - segment shape before (blue) and after (orange) lobe detection. Yellow arrowheads are existing lobes. Cyan arrowheads are newly formed lobes. The top histogram (green) depicts transfacial microtubules at the future convex cell at the lobe initiation site. The bottom histogram (magenta) depicts transfacial microtubules of the future concave cell at the lobe initiation site. Time-lapsed analysis of the occurrence and location of transfacial microtubules in six different lobing segments. **t**-**y**, The number of transfacial microtubules in the lobing cortical domain in the future convex (green) and future concave (magenta) cells. Scale bar = 5 μm.

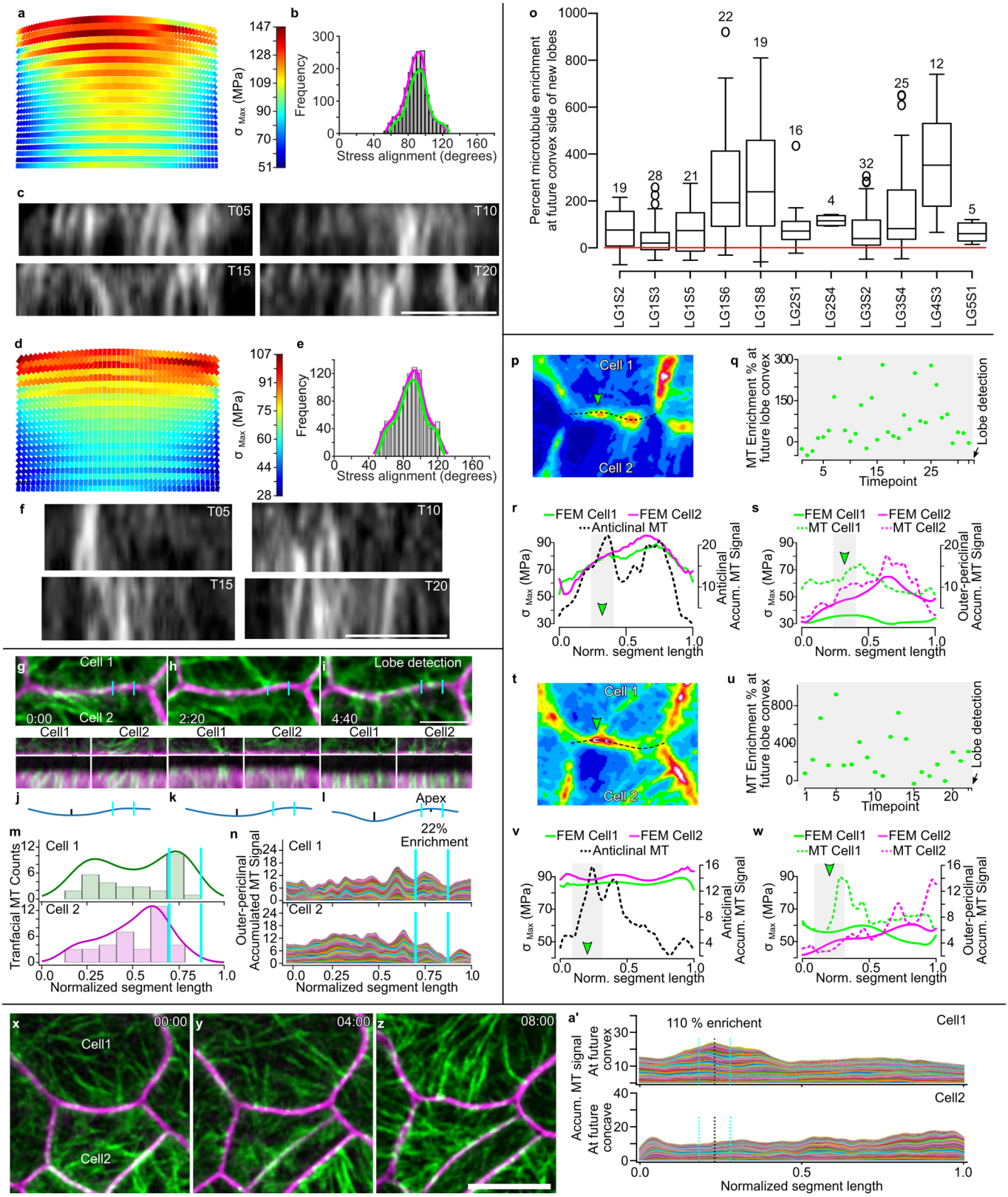

Extended Data Fig. 5 | See next page for caption.

Extended Data Fig. 5 | Cross-correlation analyses of microtubules, cell wall stress, and lobe initiation. (**a**, **d**) Heatmap of σ-max values on the anticlinal wall for two lobing segments. (**b**, **e**) Density plots of stress alignment at the anticlinal wall for cell 1 (green) and cell 2 (magenta). (**c**, **f**) Face-view of cortical microtubules at the anticlinal wall for segment depicted on A and D respectively. **g**-**i**, Time-lapse images of the plasma-membrane, (PIP2:mCherry - magenta) and microtubules (GFP:TUB6 - green) of a lobing segment that was captured for > 4 hours before the lobe was detected. **j**-**l**, Outline of the segment shape for segment corresponding to the live-cell images above where the lobe initiation cortical domain is marked using cyan vertical lines and lobes peak locations are marked by a black vertical line. **m**, Density plot of manually scored transfacial microtubules where cell 1 has a peak at the future convex side of a lobe before its detection. **n**, The accumulated microtubule signal method can detect enriched microtubule signal ($Enrichement = 1 - \frac{Area\ under\ curve_{Cell1}}{Area\ under\ curve_{Cell2}} * 100$) in cell1 within the future convex domain. **o**, Summary of outer periclinal microtubule enrichment in future convex cells measured from 11 independent lobing events. Boxplots show the distribution of microtubule enrichment of future lobe convex domain prior to lobe detection. Center lines show the medians; box limits indicate the 25th and 75th percentiles as determined by R software; whiskers extend 1.5 times the interquartile range from the 25th and 75th percentiles, outliers are represented by dots. The number of time-points at 10 min intervals is listed above each boxplot. Example images of two additional lobing pairs that could be converted to FE models and tested for MT and tensile stress correlations at sites of microtubule enrichment and lobe formation. (**p**, **t**) Summed microtubule signal projected images of segments before lobe detection. (**q**, **u**) Enrichment of microtubules at the future convex side of a lobe as a function of time before lobe detection. (**r**, **v**) Line plots of FE σ_{Max} predictions along the anticlinal wall of cell 1 (green) and cell 2 (magenta), microtubule accumulated signals along the shared anticlinal wall (black dashed line). (**s**, **w**) Line plots of FE σ_{Max} predictions along the outer periclinal wall of cell 1 (green) and cell 2 (magenta), microtubule accumulated signals outer periclinal wall of cell 1 (green dashed line) and cell 2 (magenta dashed line). Symmetry breaking events are not defined by a pre-existing segment shape. **x**-**z**, Snapshots of eight-hour time-lapse with plasma-membrane (PIP2:mCherry - magenta) and microtubule (GFP:TUB6 - green) markers of a segment that has a symmetry-breaking event against the established bulging shape. (**a'** - top) Accumulated microtubule signal plot and level of enrichment within the future convex cortical region (cell 1) (**a'** - bottom) Accumulated microtubule signal plot (cell 2). Scale bars = 5 μm for **c**, **d**, **g**–**i**; 10 μm for **x**–**z**.

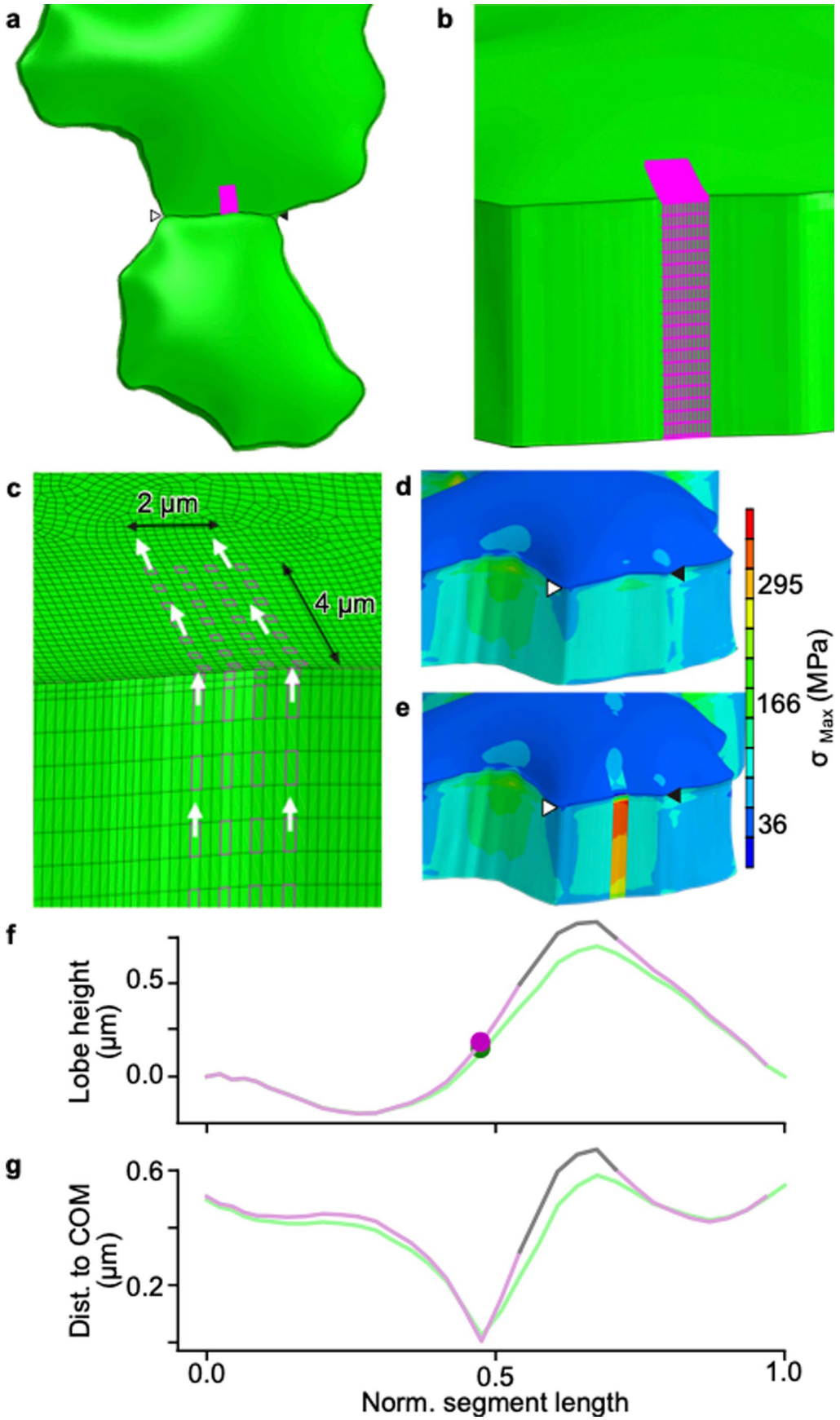

Extended Data Fig. 6 | See next page for caption.

Extended Data Fig. 6 | Localized microfibril alignment can drive lobe initiation: an FE analysis. a, Overview of a lobing pair of pavement cells. A transfacial patch of anisotropic material is located in one cell while the rest of the material in both cells is isotropic. **b**, The material in the connected anticlinal wall in the same cell is also defined as anisotropic. Note that no transition zone near the edges of the patch is used. **c**, The anisotropic patch has a width of 2μm, and the simulated MF direction is aligned with the arrows. **d**, Maximum principal stress map after pressurization and relaxation for the completely isotropic case; this result serves as a reference for the deformation. **e**, Stress map for the case which includes the anisotropic patch, which shows a stress concentration within the patch area. **f**,**g**, Comparison of the cell-cell interface geometry for the isotropic (reference – green) and anisotropic (magenta) models.

nature research

Corresponding author(s): Daniel Szymanski

Last updated by author(s): 19/04/2021

Reporting Summary

Nature Research wishes to improve the reproducibility of the work that we publish. This form provides structure for consistency and transparency in reporting. For further information on Nature Research policies, see our Editorial Policies and the Editorial Policy Checklist.

Statistics

For all statistical analyses, confirm that the following items are present in the figure legend, table legend, main text, or Methods section.

n/a	Confirmed	
☐	☒	The exact sample size (*n*) for each experimental group/condition, given as a discrete number and unit of measurement
☐	☒	A statement on whether measurements were taken from distinct samples or whether the same sample was measured repeatedly
☐	☒	The statistical test(s) used AND whether they are one- or two-sided *Only common tests should be described solely by name; describe more complex techniques in the Methods section.*
☐	☒	A description of all covariates tested
☐	☒	A description of any assumptions or corrections, such as tests of normality and adjustment for multiple comparisons
☐	☒	A full description of the statistical parameters including central tendency (e.g. means) or other basic estimates (e.g. regression coefficient) AND variation (e.g. standard deviation) or associated estimates of uncertainty (e.g. confidence intervals)
☐	☒	For null hypothesis testing, the test statistic (e.g. *F*, *t*, *r*) with confidence intervals, effect sizes, degrees of freedom and *P* value noted *Give P values as exact values whenever suitable.*
☒	☐	For Bayesian analysis, information on the choice of priors and Markov chain Monte Carlo settings
☒	☐	For hierarchical and complex designs, identification of the appropriate level for tests and full reporting of outcomes
☒	☐	Estimates of effect sizes (e.g. Cohen's *d*, Pearson's *r*), indicating how they were calculated

Our web collection on statistics for biologists contains articles on many of the points above.

Software and code

Policy information about availability of computer code

Data collection	slidebook software for confocal imaging
Data analysis	Slidebook, FiJI, Abacus for finite element modeling,

For manuscripts utilizing custom algorithms or software that are central to the research but not yet described in published literature, software must be made available to editors and reviewers. We strongly encourage code deposition in a community repository (e.g. GitHub). See the Nature Research guidelines for submitting code & software for further information.

Data

Policy information about availability of data

All manuscripts must include a data availability statement. This statement should provide the following information, where applicable:

- Accession codes, unique identifiers, or web links for publicly available datasets
- A list of figures that have associated raw data
- A description of any restrictions on data availability

FIJI macros, python scripts, and PLDP growth rates code in R are available at https://github.com/yamsissamy/naturePlant_lobeInitiation.

Field-specific reporting

Please select the one below that is the best fit for your research. If you are not sure, read the appropriate sections before making your selection.

☒ Life sciences ☐ Behavioural & social sciences ☐ Ecological, evolutionary & environmental sciences

For a reference copy of the document with all sections, see nature.com/documents/nr-reporting-summary-flat.pdf

Life sciences study design

All studies must disclose on these points even when the disclosure is negative.

Sample size	Sample size for time lapsed imaging was determined by collecting data on at least 10 independent events, then assessing the level of significance with statistical tests.
Data exclusions	Time lapse imaging data of lobe initiation was excluded in one case because the detected feature was not a true lobe but an indirect effect of a highly polarized and rapidly growing lobe in an adjacent region of the cell segment.
Replication	All experiments were replicated in at least 6 independent time lapse experiments.
Randomization	All imaging fields were selected at the base of 1.5 DAG cotyledons focusing on groups of cells that were not highly lobed and therefore were more likely to display the polarized growth behavior that was under study.
Blinding	No blinding.

Reporting for specific materials, systems and methods

We require information from authors about some types of materials, experimental systems and methods used in many studies. Here, indicate whether each material, system or method listed is relevant to your study. If you are not sure if a list item applies to your research, read the appropriate section before selecting a response.

Materials & experimental systems

n/a	Involved in the study
☐	☐ Antibodies
☐	☐ Eukaryotic cell lines
☐	☐ Palaeontology and archaeology
☐	☐ Animals and other organisms
☐	☐ Human research participants
☐	☐ Clinical data
☐	☐ Dual use research of concern

Methods

n/a	Involved in the study
☐	☐ ChIP-seq
☐	☐ Flow cytometry
☐	☐ MRI-based neuroimaging

Antibodies

Antibodies used	*Describe all antibodies used in the study; as applicable, provide supplier name, catalog number, clone name, and lot number.*
Validation	*Describe the validation of each primary antibody for the species and application, noting any validation statements on the manufacturer's website, relevant citations, antibody profiles in online databases, or data provided in the manuscript.*

Eukaryotic cell lines

Policy information about cell lines

Cell line source(s)	*State the source of each cell line used.*
Authentication	*Describe the authentication procedures for each cell line used OR declare that none of the cell lines used were authenticated.*
Mycoplasma contamination	*Confirm that all cell lines tested negative for mycoplasma contamination OR describe the results of the testing for mycoplasma contamination OR declare that the cell lines were not tested for mycoplasma contamination.*
Commonly misidentified lines (See ICLAC register)	*Name any commonly misidentified cell lines used in the study and provide a rationale for their use.*

Palaeontology and Archaeology

Specimen provenance	*Provide provenance information for specimens and describe permits that were obtained for the work (including the name of the issuing authority, the date of issue, and any identifying information).*
Specimen deposition	*Indicate where the specimens have been deposited to permit free access by other researchers.*
Dating methods	*If new dates are provided, describe how they were obtained (e.g. collection, storage, sample pretreatment and measurement), where they were obtained (i.e. lab name), the calibration program and the protocol for quality assurance OR state that no new dates are provided.*

☐ Tick this box to confirm that the raw and calibrated dates are available in the paper or in Supplementary Information.

Ethics oversight	*Identify the organization(s) that approved or provided guidance on the study protocol, OR state that no ethical approval or guidance was required and explain why not.*

Note that full information on the approval of the study protocol must also be provided in the manuscript.

Animals and other organisms

Policy information about studies involving animals; ARRIVE guidelines recommended for reporting animal research

Laboratory animals	*For laboratory animals, report species, strain, sex and age OR state that the study did not involve laboratory animals.*
Wild animals	*Provide details on animals observed in or captured in the field; report species, sex and age where possible. Describe how animals were caught and transported and what happened to captive animals after the study (if killed, explain why and describe method; if released, say where and when) OR state that the study did not involve wild animals.*
Field-collected samples	*For laboratory work with field-collected samples, describe all relevant parameters such as housing, maintenance, temperature, photoperiod and end-of-experiment protocol OR state that the study did not involve samples collected from the field.*
Ethics oversight	*Identify the organization(s) that approved or provided guidance on the study protocol, OR state that no ethical approval or guidance was required and explain why not.*

Note that full information on the approval of the study protocol must also be provided in the manuscript.

Human research participants

Policy information about studies involving human research participants

Population characteristics	*Describe the covariate-relevant population characteristics of the human research participants (e.g. age, gender, genotypic information, past and current diagnosis and treatment categories). If you filled out the behavioural & social sciences study design questions and have nothing to add here, write "See above."*
Recruitment	*Describe how participants were recruited. Outline any potential self-selection bias or other biases that may be present and how these are likely to impact results.*
Ethics oversight	*Identify the organization(s) that approved the study protocol.*

Note that full information on the approval of the study protocol must also be provided in the manuscript.

Clinical data

Policy information about clinical studies

All manuscripts should comply with the ICMJE guidelines for publication of clinical research and a completed CONSORT checklist must be included with all submissions.

Clinical trial registration	*Provide the trial registration number from ClinicalTrials.gov or an equivalent agency.*
Study protocol	*Note where the full trial protocol can be accessed OR if not available, explain why.*
Data collection	*Describe the settings and locales of data collection, noting the time periods of recruitment and data collection.*
Outcomes	*Describe how you pre-defined primary and secondary outcome measures and how you assessed these measures.*

Dual use research of concern

Policy information about dual use research of concern

Hazards

Could the accidental, deliberate or reckless misuse of agents or technologies generated in the work, or the application of information presented in the manuscript, pose a threat to:

No	Yes	
☒	☐	Public health
☒	☐	National security
☒	☐	Crops and/or livestock
☒	☐	Ecosystems
☒	☐	Any other significant area

Experiments of concern

Does the work involve any of these experiments of concern:

No	Yes	
☒	☐	Demonstrate how to render a vaccine ineffective
☒	☐	Confer resistance to therapeutically useful antibiotics or antiviral agents
☒	☐	Enhance the virulence of a pathogen or render a nonpathogen virulent
☒	☐	Increase transmissibility of a pathogen
☒	☐	Alter the host range of a pathogen
☒	☐	Enable evasion of diagnostic/detection modalities
☒	☐	Enable the weaponization of a biological agent or toxin
☒	☐	Any other potentially harmful combination of experiments and agents

ChIP-seq

Data deposition

☐ Confirm that both raw and final processed data have been deposited in a public database such as GEO.

☐ Confirm that you have deposited or provided access to graph files (e.g. BED files) for the called peaks.

Data access links *May remain private before publication.*	*For "Initial submission" or "Revised version" documents, provide reviewer access links. For your "Final submission" document, provide a link to the deposited data.*
Files in database submission	*Provide a list of all files available in the database submission.*
Genome browser session (e.g. UCSC)	*Provide a link to an anonymized genome browser session for "Initial submission" and "Revised version" documents only, to enable peer review. Write "no longer applicable" for "Final submission" documents.*

Methodology

Replicates	*Describe the experimental replicates, specifying number, type and replicate agreement.*
Sequencing depth	*Describe the sequencing depth for each experiment, providing the total number of reads, uniquely mapped reads, length of reads and whether they were paired- or single-end.*
Antibodies	*Describe the antibodies used for the ChIP-seq experiments; as applicable, provide supplier name, catalog number, clone name, and lot number.*
Peak calling parameters	*Specify the command line program and parameters used for read mapping and peak calling, including the ChIP, control and index files used.*
Data quality	*Describe the methods used to ensure data quality in full detail, including how many peaks are at FDR 5% and above 5-fold enrichment.*
Software	*Describe the software used to collect and analyze the ChIP-seq data. For custom code that has been deposited into a community repository, provide accession details.*

Flow Cytometry

Plots

Confirm that:

☐ The axis labels state the marker and fluorochrome used (e.g. CD4-FITC).

☐ The axis scales are clearly visible. Include numbers along axes only for bottom left plot of group (a 'group' is an analysis of identical markers).

☐ All plots are contour plots with outliers or pseudocolor plots.

☐ A numerical value for number of cells or percentage (with statistics) is provided.

Methodology

Sample preparation	*Describe the sample preparation, detailing the biological source of the cells and any tissue processing steps used.*
Instrument	*Identify the instrument used for data collection, specifying make and model number.*
Software	*Describe the software used to collect and analyze the flow cytometry data. For custom code that has been deposited into a community repository, provide accession details.*
Cell population abundance	*Describe the abundance of the relevant cell populations within post-sort fractions, providing details on the purity of the samples and how it was determined.*
Gating strategy	*Describe the gating strategy used for all relevant experiments, specifying the preliminary FSC/SSC gates of the starting cell population, indicating where boundaries between "positive" and "negative" staining cell populations are defined.*

☐ Tick this box to confirm that a figure exemplifying the gating strategy is provided in the Supplementary Information.

Magnetic resonance imaging

Experimental design

Design type	*Indicate task or resting state; event-related or block design.*
Design specifications	*Specify the number of blocks, trials or experimental units per session and/or subject, and specify the length of each trial or block (if trials are blocked) and interval between trials.*
Behavioral performance measures	*State number and/or type of variables recorded (e.g. correct button press, response time) and what statistics were used to establish that the subjects were performing the task as expected (e.g. mean, range, and/or standard deviation across subjects).*

Acquisition

Imaging type(s)	*Specify: functional, structural, diffusion, perfusion.*
Field strength	*Specify in Tesla*
Sequence & imaging parameters	*Specify the pulse sequence type (gradient echo, spin echo, etc.), imaging type (EPI, spiral, etc.), field of view, matrix size, slice thickness, orientation and TE/TR/flip angle.*
Area of acquisition	*State whether a whole brain scan was used OR define the area of acquisition, describing how the region was determined.*

Diffusion MRI ☐ Used ☐ Not used

Preprocessing

Preprocessing software	*Provide detail on software version and revision number and on specific parameters (model/functions, brain extraction, segmentation, smoothing kernel size, etc.).*
Normalization	*If data were normalized/standardized, describe the approach(es): specify linear or non-linear and define image types used for transformation OR indicate that data were not normalized and explain rationale for lack of normalization.*
Normalization template	*Describe the template used for normalization/transformation, specifying subject space or group standardized space (e.g. original Talairach, MNI305, ICBM152) OR indicate that the data were not normalized.*
Noise and artifact removal	*Describe your procedure(s) for artifact and structured noise removal, specifying motion parameters, tissue signals and physiological signals (heart rate, respiration).*

Volume censoring

Define your software and/or method and criteria for volume censoring, and state the extent of such censoring.

Statistical modeling & inference

Model type and settings

Specify type (mass univariate, multivariate, RSA, predictive, etc.) and describe essential details of the model at the first and second levels (e.g. fixed, random or mixed effects; drift or auto-correlation).

Effect(s) tested

Define precise effect in terms of the task or stimulus conditions instead of psychological concepts and indicate whether ANOVA or factorial designs were used.

Specify type of analysis: ☐ Whole brain ☐ ROI-based ☐ Both

Statistic type for inference
(See Eklund et al. 2016)

Specify voxel-wise or cluster-wise and report all relevant parameters for cluster-wise methods.

Correction

Describe the type of correction and how it is obtained for multiple comparisons (e.g. FWE, FDR, permutation or Monte Carlo).

Models & analysis

n/a	Involved in the study
☐	☐ Functional and/or effective connectivity
☐	☐ Graph analysis
☐	☐ Multivariate modeling or predictive analysis

Functional and/or effective connectivity

Report the measures of dependence used and the model details (e.g. Pearson correlation, partial correlation, mutual information).

Graph analysis

Report the dependent variable and connectivity measure, specifying weighted graph or binarized graph, subject- or group-level, and the global and/or node summaries used (e.g. clustering coefficient, efficiency, etc.).

Multivariate modeling and predictive analysis

Specify independent variables, features extraction and dimension reduction, model, training and evaluation metrics.